EUROPEAN ORGANIZATION FOR NUCLEAR RESEARCH (CERN)

CERN-EP-2022-112
2022/07/05

CMS-TOP-21-008

Measurement of the top quark pole mass using $\mathrm{t\bar{t}}$+jet events in the dilepton final state in proton-proton collisions at $\sqrt{s} = 13\,\mathrm{TeV}$

The CMS Collaboration

Abstract

A measurement of the top quark pole mass $m_{\mathrm{t}}^{\mathrm{pole}}$ in events where a top quark-antiquark pair ($\mathrm{t\bar{t}}$) is produced in association with at least one additional jet ($\mathrm{t\bar{t}}$+jet) is presented. This analysis is performed using proton-proton collision data at $\sqrt{s} = 13\,\mathrm{TeV}$ collected by the CMS experiment at the CERN LHC, corresponding to a total integrated luminosity of $36.3\,\mathrm{fb}^{-1}$. Events with two opposite-sign leptons in the final state ($\mathrm{e^+e^-}$, $\mu^+\mu^-$, $\mathrm{e}^{\pm}\mu^{\mp}$) are analyzed. The reconstruction of the main observable and the event classification are optimized using multivariate analysis techniques based on machine learning. The production cross section is measured as a function of the inverse of the invariant mass of the $\mathrm{t\bar{t}}$+jet system at the parton level using a maximum likelihood unfolding. Given a reference parton distribution function (PDF), the top quark pole mass is extracted using the theoretical predictions at next-to-leading order. For the ABMP16NLO PDF, this results in $m_{\mathrm{t}}^{\mathrm{pole}} = 172.94 \pm 1.37\,\mathrm{GeV}$.

Submitted to the Journal of High Energy Physics

1 Introduction

The top quark is the most massive elementary particle known. Its mass m_t is a free parameter of the standard model (SM) Lagrangian and is an input to the global electroweak fits [1–4] and calculations of the Higgs boson self-coupling [5, 6]. The value of m_t needs to be determined experimentally. Direct measurements of m_t at hadron colliders, being dominated by measurements in proton-proton (pp) collisions at the CERN LHC, reach a precision on the order of 0.5 GeV [7–14]. The combined value of measurements by the CMS Collaboration at $\sqrt{s} = 7$ and 8 TeV is $m_t = 172.44 \pm 0.48$ GeV [10]. The direct measurements rely on the reconstruction of the top quark kinematic variables from its decay products and hence on the modeling provided by multipurpose Monte Carlo (MC) event generators. These generators typically make use of parton shower models to approximate higher-order effects, while heuristic models tuned to the data are used to describe the color neutralization in the nonperturbative regime and the underlying event (UE). This introduces ambiguities in the interpretation of the top quark mass assumed in the simulation, m_t^{MC}. An additional intrinsic uncertainty on the order of about 0.5–1 GeV is expected when interpreting a direct measurement of m_t^{MC} in terms of the top quark pole mass, m_t^{pole} [15–22].

Alternatively, the value of m_t can be extracted by comparing cross section measurements to fixed-order theoretical predictions in well-defined renormalization schemes. The value of m_t^{pole} was measured by both the ATLAS and CMS Collaborations [23–29], reaching an uncertainty below 1 GeV in a recent CMS measurement [29] by using the multidifferential cross sections of top quark-antiquark ($t\bar{t}$) pair production. The top quark mass defined in the modified minimal subtraction ($\overline{MS}$) scheme, referred to as the top quark running mass, was also measured [22, 30, 31] and its energy scale dependence was investigated in Ref. [32].

In this paper, the value of m_t^{pole} is measured by using the normalized differential cross section of $t\bar{t}$ production in association with at least one energetic jet ($t\bar{t}$+jet) [33]. The measurement follows the approach developed in Refs. [31, 33, 34], where the normalized differential $t\bar{t}$+jet cross section is measured as a function of the ρ observable, defined as

$$\rho = \frac{2m_0}{m_{t\bar{t}+jet}}, \tag{1}$$

where $m_{t\bar{t}+jet}$ is the invariant mass of the $t\bar{t}$+jet system. The result of the measurement does not depend on the choice of the scaling constant m_0, which is set to $m_0 = 170$ GeV, as used in previous measurements. The sensitivity to m_t is enhanced as compared to $t\bar{t}$ production due to the presence of an additional jet because the kinematic parameters of the radiated gluons in $t\bar{t}$+jet events depend on the mass of the top quark. High sensitivity to m_t^{pole} is expected close to the production threshold, for $\rho > 0.65$, while for high $m_{t\bar{t}+jet}$, e.g., $\rho < 0.55$, this sensitivity is small. Such a measurement was performed by the ATLAS Collaboration using pp collision data at $\sqrt{s} = 7$ and 8 TeV [26, 35], corresponding to integrated luminosities of 4.6 and 20.2 fb^{-1}, respectively, finding a value of $m_t^{pole} = 171.1\,^{+1.2}_{-1.0}$ GeV.

In this paper, a measurement of m_t^{pole} is made by using the ρ dependence at the center-of-mass energy of 13 TeV. The data were recorded by the CMS detector in 2016, corresponding to an integrated luminosity of 36.3 fb^{-1}.

In this analysis, the normalized differential cross section is measured at the detector level and is unfolded to the parton level. The unfolding is performed via the maximum likelihood method with profiled nuisance parameters for all systematic uncertainties, following the approach de-

veloped in Ref. [32]. The signal and background processes are fitted simultaneously, and the systematic uncertainties and their correlations are determined from data. This leads to significantly improved experimental precision over classical approaches where systematic uncertainties are not profiled [22].

The paper is structured as follows. After a brief description of the CMS experiment and the event reconstruction in Section 2, the data sets and simulation are presented in Section 3, together with the definition of the signal. The event selection is explained in Section 4. In Section 5, a detailed description of multivariate analysis techniques developed for this measurement is given. The maximum likelihood fit for the signal extraction and unfolding is described in Section 6, followed by a discussion of the systematic uncertainties in Section 7. The determination of $m_{\mathrm{t}}^{\mathrm{pole}}$ is presented in Section 8, and a summary is given in Section 9. Tabulated results are provided in the HEPData record for this analysis [36].

2 The CMS detector and event reconstruction

The central feature of the CMS apparatus is a superconducting solenoid of 6 m internal diameter, providing a magnetic field of 3.8 T. Within the solenoid volume are a silicon pixel and strip tracker, a lead tungstate crystal electromagnetic calorimeter (ECAL), and a brass and scintillator hadron calorimeter (HCAL), each composed of a barrel and two endcap sections. Forward calorimeters extend the pseudorapidity (η) coverage provided by the barrel and endcap detectors. Muons are detected in gas-ionization chambers embedded in the steel flux-return yoke outside the solenoid. Events of interest are selected using a two-tiered trigger system. The first level (L1), composed of custom hardware processors, uses information from the calorimeters and muon detectors to select events at a rate of around 100 kHz within a fixed latency of about 4 μs [37]. The second level, known as the high-level trigger (HLT), consists of a farm of processors running a version of the full event reconstruction software optimized for fast processing, and reduces the event rate to around 1 kHz before data storage [38]. A more detailed description of the CMS detector, together with a definition of the coordinate system used and the relevant kinematic variables, can be found in Ref. [39].

The primary vertex (PV) is taken to be the vertex corresponding to the hardest scattering in the event, evaluated using tracking information alone, as described in Section 9.4.1 of Ref. [40].

The particle-flow (PF) algorithm [41] aims to reconstruct and identify each individual particle in an event, with an optimized combination of information from the various elements of the CMS detector. The energy of photons is obtained from the ECAL measurement. The energy of electrons is determined from a combination of the electron momentum at the PV as determined by the tracker, the energy of the corresponding ECAL cluster, and the energy sum of all bremsstrahlung photons spatially compatible with originating from the electron track. The energy of muons is obtained from the curvature of the corresponding track. The energy of charged hadrons is determined from a combination of their momentum measured in the tracker and the matching ECAL and HCAL energy deposits, corrected for the response function of the calorimeters to hadronic showers. Finally, the energy of neutral hadrons is obtained from the corresponding corrected ECAL and HCAL energies.

For each event, hadronic jets are clustered from PF particles using the infrared- and collinear-safe anti-k_{T} algorithm with a distance parameter of 0.4. Jet momentum is determined as the vectorial sum of all particle momenta in the jet, and is found from simulation to be, on average, within 5 to 10% of the true momentum over the whole transverse momentum (p_{T}) spectrum and detector acceptance. Additional pp interactions within the same or nearby bunch crossings

(pileup) can contribute additional tracks and calorimetric energy depositions, increasing the apparent jet momentum. To mitigate this effect, tracks identified to be originating from pileup vertices are discarded and an offset correction is applied to correct for remaining contributions. Jet energy corrections are derived from simulation studies so that the average measured energy of jets becomes identical to that of particle-level jets. In situ measurements of the momentum balance in dijet, photon+jet, Z+jet, and multijet events are used to determine any residual differences between the jet energy scale in data and in simulation, and appropriate corrections are made [42]. No dedicated flavor-dependent corrections are made. Additional selection criteria are applied to each jet to remove jets potentially dominated by instrumental effects or reconstruction failures. The jet energy resolution amounts typically to 15–20% at 30 GeV, 10% at 100 GeV, and 5% at 1 TeV [42].

The missing transverse momentum vector $\vec{p}_{\mathrm{T}}^{\,\mathrm{miss}}$ is computed as the negative vector sum of the $\vec{p}_{\mathrm{T}}$ of all the PF candidates in an event, and its magnitude is denoted as $p_{\mathrm{T}}^{\mathrm{miss}}$ [43]. The value of $\vec{p}_{\mathrm{T}}^{\,\mathrm{miss}}$ is modified to account for corrections to the energy scale of the reconstructed jets in the event. A pileup per particle identification algorithm [44, 45] is applied to reduce the pileup dependence of $\vec{p}_{\mathrm{T}}^{\,\mathrm{miss}}$ and the PF candidates are weighted by their probability to originate from the PV [43].

Electrons are measured in the range $|\eta| < 2.5$ and the single-electron efficiency is about 80%. The electron momenta are estimated by combining energy measurements in the ECAL with momentum measurements in the tracker [46]. The efficiency to reconstruct and identify electrons is better than 95% [47]. The momentum resolution for electrons with $p_{\mathrm{T}} \approx 45$ GeV from $\mathrm{Z} \to \mathrm{ee}$ decays ranges from 1.6 to 5%. It is generally better in the barrel region ($|\eta| < 1.479$) than in the endcaps ($1.479 < |\eta| < 3.0$), and also depends on the bremsstrahlung energy emitted by the electron as it traverses the material in front of the ECAL [46, 47].

Muons are measured in the range $|\eta| < 2.4$, with detection planes made using three technologies: drift tubes, cathode strip chambers, and resistive plate chambers. The single-muon trigger efficiency exceeds 90% over the full η range, and the efficiency to reconstruct and identify muons is greater than 96%. Matching muons to tracks measured in the silicon tracker results in a relative p_{T} resolution, for muons with p_{T} up to 100 GeV, of 1% in the barrel and 3% in the endcaps. The p_{T} resolution in the barrel is better than 7% for muons with p_{T} up to 1 TeV [48].

3 Data samples and event simulation

The analysis uses pp collision data recorded by the CMS experiment in 2016, corresponding to an integrated luminosity of $36.3\,\mathrm{fb}^{-1}$. The events are required to pass several HLT selection criteria, including the presence of either one or two leptons (electrons or muons). The single-electron (muon) trigger requires a minimum p_{T} of 27 (24) GeV. In the case of the dielectron triggers, at least two lepton candidates with a minimum p_{T} of 23 and 12 GeV are required, while for the dimuon triggers the respective thresholds are 17 and 8 GeV. For the electron-muon triggers, the selection requirements are $p_{\mathrm{T}} > 23$ GeV and $p_{\mathrm{T}} > 8$ GeV ($p_{\mathrm{T}} > 13$ GeV) if the muon (electron) is the lepton with higher p_{T}.

Signal and background $\mathrm{t\bar{t}}$ processes are simulated using the POWHEG (version 2) [49–51] MC generator at next-to-leading order (NLO) in quantum chromodynamics (QCD) for the matrix element (ME) calculations. The top quark mass in the simulation is fixed to $m_{\mathrm{t}}^{\mathrm{MC}} = 172.5$ GeV and the proton structure is described using the NNPDF 3.1 PDF at next-to-NLO (NNLO) [52, 53]. Parton showering is performed using PYTHIA (version 8.230) [54] with the CP5 tune [55]. The h_{damp} parameter in POWHEG, which effectively regulates the matching scale to the parton

shower, is set to $h_{\text{damp}} = 1.379 m_{\text{t}}^{\text{MC}}$ [55]. The $\mathrm{t\bar{t}}$ simulation is split into different components, modeling the signal and the background contributions, as described in Section 3.1.

Additionally, simulated samples of the $\mathrm{t\bar{t}}$ process are generated with up to two extra partons at the NLO ME level using MADGRAPH5_aMC@NLO [56]. These are used to derive the calibrations of the neural networks (NNs), as discussed in Section 5. Events are matched using the FxFx [57] prescription to the PYTHIA parton shower, while MADSPIN [58] is used to model the decays of the top quark and antiquark at leading order (LO).

The background contributions arise from single top quark production in association with a W boson (tW), Z/γ^* or W bosons produced with additional jets (Z+jets, W+jets), and diboson production (WW, WZ, ZZ). The contributions from the diboson and W+jets production processes are labeled as "Other" in the figures. For all the background samples, PYTHIA is used to model the parton showering, hadronization, and multiparton interactions. The tW process is simulated using POWHEG [59, 60] at NLO with the same tune and modeling parameters as used for the $\mathrm{t\bar{t}}$ process. The CUETP8M1 [61–63] tune is used for the background simulation. The Z+jets process is simulated using MADGRAPH5_aMC@NLO at LO with up to four additional partons at ME level, and is matched to the PYTHIA parton shower using the MLM [64, 65] prescription. Similarly, W+jets samples are produced using MADGRAPH5_aMC@NLO at LO with up to four additional partons at ME level. To derive the NN calibrations, an independent Z+jets simulation is generated with MADGRAPH5_aMC@NLO at NLO using the FxFx merging prescription. Diboson production is simulated at LO with PYTHIA.

All predictions are normalized to their theoretical cross section and the corresponding integrated luminosity of the data set. For the $\mathrm{t\bar{t}}$ signal, the value of the cross section is $830.91\,^{+20.39}_{-29.96}\,(\text{scale})\,^{+3.92}_{-3.83}\,(\text{PDF}+\alpha_{\text{S}})$ pb, as calculated with the TOP++ (version 2.0) program [66] at NNLO precision. The calculation assumes $m_{\text{t}} = 172.5\,\text{GeV}$, makes use of the NNPDF3.1 PDF set at NNLO, and includes the resummation of next-to-next-to-leading-logarithmic soft-gluon terms [67–72]. The labels "scale" and α_{S} refer to the uncertainty assessed by varying the renormalization (μ_{R}) and factorization (μ_{F}) scales and the value for the strong coupling constant, respectively. The remaining cross sections are calculated at approximate NNLO for tW production [73], NLO for Z+jets and diboson production [74], and NNLO for W+jets [75] production.

For all simulated samples, the CMS detector response is simulated with GEANT4 [76]. To model the effect of pileup, additional minimum-bias interactions are added to the simulated events. Weights are used with the simulated events to reproduce the pileup distribution in the data. The weights are estimated from the measured bunch-to-bunch instantaneous luminosity, assuming a total inelastic pp cross section of 69.2 mb [77].

3.1 Signal definition at the parton level

The simulated signal consists of $\mathrm{t\bar{t}}$ events in which a dilepton and at least one jet emitted at the parton level with $p_{\text{T}} > 30\,\text{GeV}$ and $|\eta| < 2.4$ are produced. The parton level is defined after parton showering with on-shell top quarks. Additional jets are clustered by applying the anti-k_{T} algorithm [78, 79] with a distance parameter of 0.4, using all particles before hadronization that do not stem from the top quark decays. The $\mathrm{t\bar{t}}$+jet signal is obtained from the nominal $\mathrm{t\bar{t}}$ simulation by selecting events with at least one additional parton-level jet passing the selection described above. The remaining events are considered as background and labeled as $\mathrm{t\bar{t}}$+0 jet. The $\mathrm{t\bar{t}}$+jet signal is further split into subprocesses that are defined based on the value of ρ at parton level in the following binning: 0–0.3, 0.3–0.45, 0.45–0.7, and 0.7–1. The binning choice is explained in Section 6. The simulated $\mathrm{t\bar{t}}$ signal demands at least two leptons, including those

from the decays of tau leptons. The remaining $\mathrm{t\bar{t}}$ events are considered as background. The unfolded results are extrapolated to the full phase space using the $\mathrm{t\bar{t}}$ MC simulation.

4 Event selection

Data events containing two opposite-sign leptons ($\mathrm{e^+e^-}$, $\mu^+\mu^-$, $\mathrm{e^\pm}\mu^\mp$) are selected. To suppress events from low-mass resonance decays and the Drell-Yan process, the dilepton invariant mass ($m_{\ell\ell}$) is required to be larger than 20 GeV. The Z+jets background contribution is reduced by discarding events with $p_{\mathrm{T}}^{\mathrm{miss}} < 40$ GeV and $m_{\ell\ell}$ in the Z mass window between 76 and 106 GeV, for the same-flavor lepton channels.

The leading (subleading) electron candidate is required to have $p_{\mathrm{T}} > 25$ (20) GeV and $|\eta| < 2.4$. Electrons reconstructed in the ECAL barrel-endcap transition region ($1.44 < |\eta| < 1.57$) are rejected. A relative isolation parameter (I_{rel}) is calculated for each electron candidate, defined as the ratio of the p_{T} sum of neutral and charged hadron and photon PF candidates, within a distance of $\Delta R = \sqrt{(\Delta\eta)^2 + (\Delta\phi)^2} = 0.3$ in η-ϕ space, to the p_{T} of the electron candidate, where ϕ is the azimuthal angle. Depending on the electron p_{T}, the maximum allowed value for I_{rel} varies from 0.05 to 0.1. Additional corrections are made to remove contributions from pileup [47]. To reject misidentified electron candidates and photon conversions, additional identification requirements are imposed [47].

Muon candidates are selected with the same p_{T} and η requirements as for the electrons, except for removing the transition-region requirement. An isolation requirement of $I_{\mathrm{rel}} < 0.15$ is applied, where all particle momenta within a distance of $\Delta R < 0.4$ from the muon are considered and pileup effects are taken into account. Muon candidates are further identified by their specific signature in the detector [48].

Jets with $p_{\mathrm{T}} > 30$ GeV and $|\eta| < 2.4$ are selected, and the value of ΔR between the jet and the selected lepton candidates must be greater than 0.4. To further reject jets arising from pileup interactions, a dedicated pileup jet identification algorithm [45] is employed for jets with p_{T} between 30 and 50 GeV. Jets originating from the hadronization of b quarks (called b jets) are identified (tagged) using the DEEPCSV algorithm [80], which makes use of associated track and secondary-vertex information as inputs to a deep NN. The chosen operating point for the discriminator has an efficiency of about 80–90% for b jets, for misidentification ("mistag") rates of 10 and 40% for light-quark and c quark jets, respectively [80]. The energy measurement of b jets is improved by about 6–12% using a deep NN estimator [81].

Lepton trigger and identification efficiencies, lepton momentum resolutions, and b tagging efficiencies are corrected in simulation to match the values in data.

The typical purities for the $\mathrm{t\bar{t}}$+jet signal obtained without requirements on the jet or b jet multiplicity range from about 15% in the $\mathrm{e^+e^-}$ and $\mu^+\mu^-$ channels to about 30% in the $\mathrm{e^\pm}\mu^\mp$ channel. When selecting only events with at least three reconstructed jets, of which one is b tagged, the purity is around 75%.

Figures 1 and 2 show the distributions of several kinematic observables from data and simulation for the combined dilepton candidates. In general, the MC simulation describes the data well. A small discrepancy between the normalization of the data and simulation is observed in several of the distributions. However, this does not affect this measurement since the normalization is determined from the likelihood fit, as described in Section 6, and the normalized cross section is used to extract $m_{\mathrm{t}}^{\mathrm{pole}}$. Some trends can be observed in the jet and lepton momentum distributions, where the spectrum predicted by the simulation has a higher average value

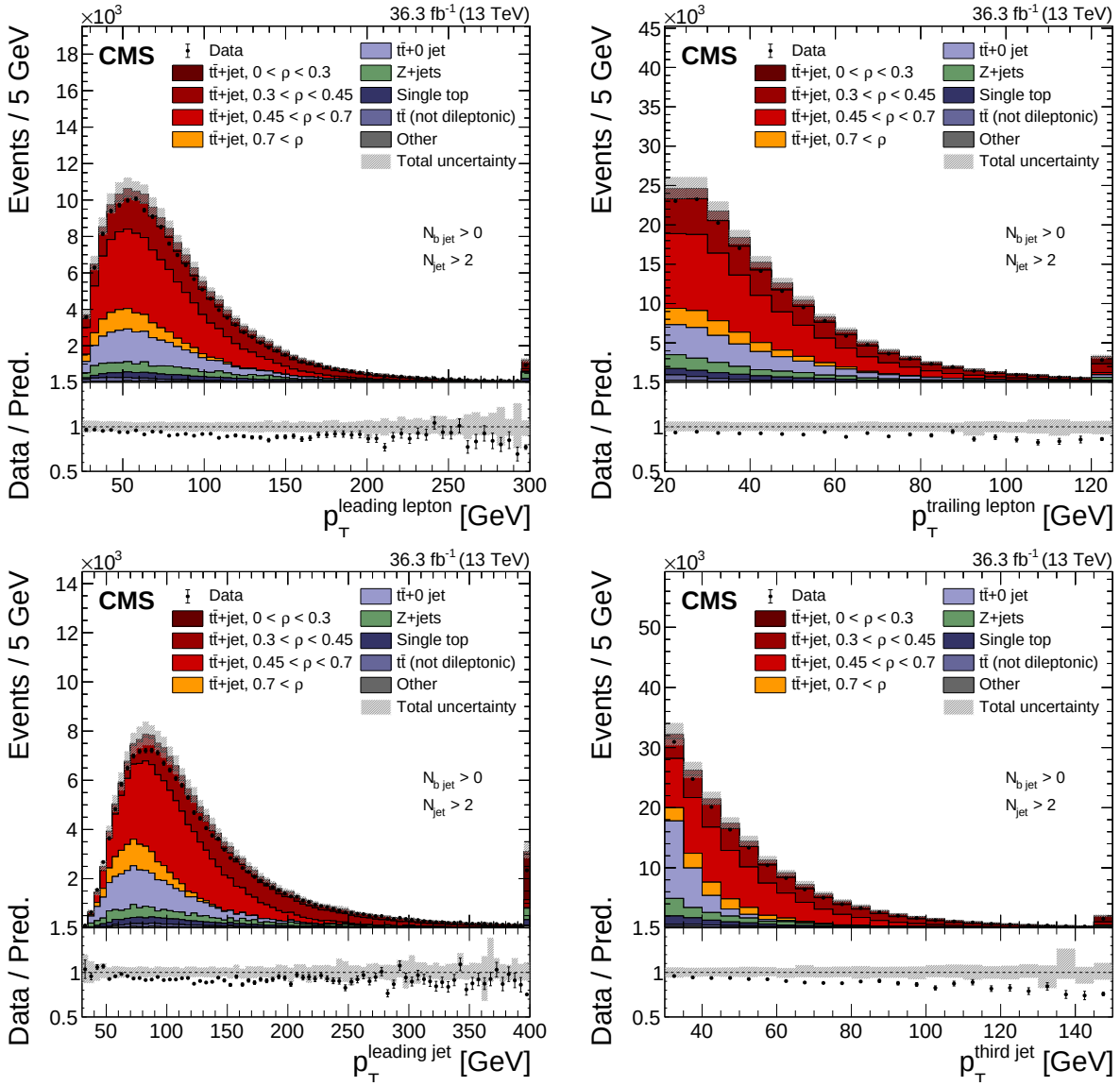

Figure 1: The observed (points) and predicted (stacked histograms) signal and background yields as a function of the leading (upper left) and subleading (upper right) lepton p_{T} and leading (lower left) and third-highest (lower right) jet p_{T} after applying the signal selection. The vertical bars on the points represent the statistical uncertainty in the data. The hatched band represents the total uncertainty in the sum of the simulated signal and background predictions. The lower panels show the ratio of the data to the sum of the signal and background predictions.

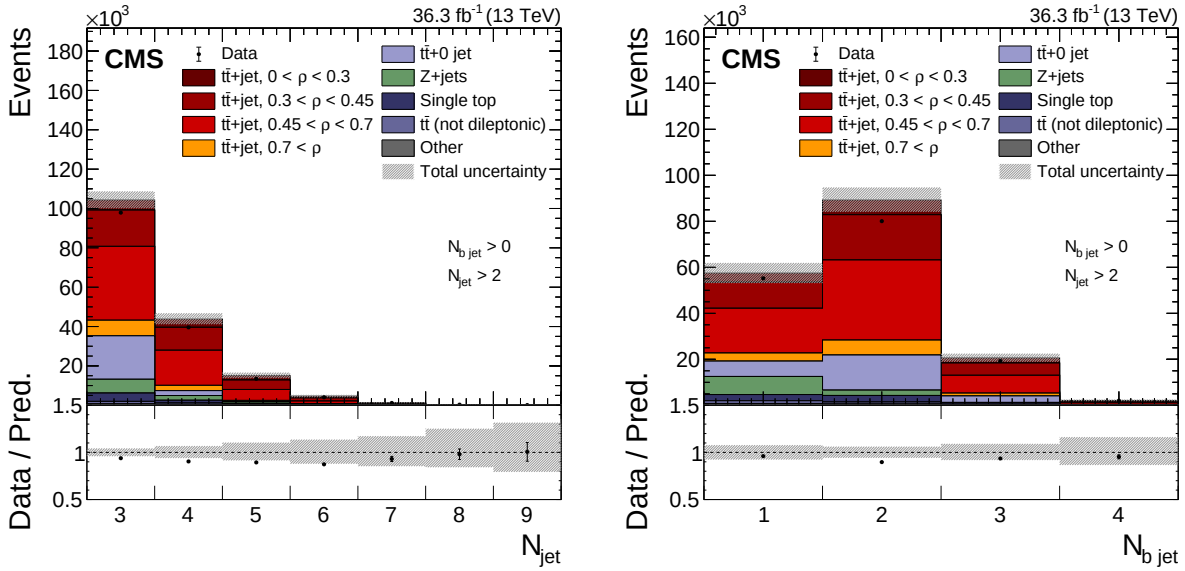

Figure 2: The observed (points) and predicted (stacked histograms) signal and background yields as a function of the jet (left), and b jet (right) multiplicities, after applying the signal selection. The vertical bars on the points represent the statistical uncertainty in the data. The hatched band represents the total uncertainty in the sum of the simulated signal and background predictions. The lower panels show the ratio of the data to the sum of the signal and background predictions.

than the one observed in data. The effect is related to the modeling of the top quark p_T in the POWHEG+PYTHIA8$t\bar{t}$ simulation, and similar observations have been made in previous measurements [82–85] when comparing the measured distributions to detector- or particle-level predictions. The jet multiplicity and b jet multiplicities from data are well described by the simulation within the total uncertainties.

5 Multivariate analysis

In this analysis, the measurement of the $t\bar{t}$+jet cross section with the largest possible acceptance is achieved by employing a profile-likelihood approach. Thus, the extrapolation effects are small and the migrations and uncertainties affecting both the normalization and shape of the final-state distributions can be kept under control.

To reconstruct ρ as the variable of interest, kinematic reconstruction techniques must be employed. These methods typically rely on imposing constraints to reconstruct the longitudinal components of the momenta of the two neutrinos from the W boson leptonic decays in $t\bar{t}$ events containing dileptons. Several methods have been established and used in previous differential $t\bar{t}$ cross section measurements [29, 32, 82–86].

Two multivariate analysis (MVA) approaches are developed to mitigate constraints on the kinematic reconstruction and and improve the signal-versus-background discrimination. The MVA methods developed for this analysis are described below.

5.1 Reconstruction of top quark kinematic variables

Two analytical kinematic reconstruction approaches referred to as "full kinematic reconstruction" and "loose kinematic reconstruction" are used. Solutions of both methods are considered as inputs to the MVAs. For the full kinematic reconstruction, the four-momenta of the top

quark and antiquark are determined using the following constraints: total $\vec{p}_{\mathrm{T}}$ conservation; the mass of the W boson (80.4 GeV), and the masses of the top quark and antiquark (172.5 GeV). Reconstructed $\vec{p}_{\mathrm{T}}^{\,\mathrm{miss}}$ in the event is assumed to originate from the two neutrinos produced in the two W boson decays. Possible ambiguities in the algebraic solutions are solved by taking the solution with the smallest $\mathrm{t\bar{t}}$ invariant mass. To increase the reconstruction efficiency and account for the detector resolution, the reconstruction procedure is repeated 100 times for each event. Each time, reconstructed momenta of the measured jets and leptons are randomly smeared according to their resolution, where the smearing effect is propagated to $\vec{p}_{\mathrm{T}}^{\,\mathrm{miss}}$. Each of the 100 solutions is weighted based on the true distribution of the invariant mass of a lepton and a b jet ($m_{\ell\mathrm{b}}$) stemming from the top quark decays as given by the simulation, where the weights for both decay chains of the t and $\bar{\mathrm{t}}$ are multiplied. All combinations of jets and leptons with $m_{\ell\mathrm{b}} < 180$ GeV are considered and ranked by the presence of b jets in the solutions, where solutions with a higher b jet multiplicity are preferred. Further details about the reconstruction method can be found in Ref. [82].

In the loose kinematic reconstruction [29], only the $\mathrm{t\bar{t}}$ system as a whole is reconstructed. The advantage of this method is that the m_{t} constraint is not used, which makes this method especially useful for the determination of m_{t}. Similarly to the full kinematic reconstruction, jet–lepton combinations with $m_{\ell\mathrm{b}} < 180$ GeV are considered and combinations including b jets are preferred over solutions without b jets. The kinematic variables of the $\nu\bar{\nu}$ system are obtained as follows: $\vec{p}_{\mathrm{T}}^{\,\nu\bar{\nu}}$ is set equal to $\vec{p}_{\mathrm{T}}^{\,\mathrm{miss}}$ and its longitudinal component and energy are set equal to that of the charged-lepton-pair system. Furthermore, constraints are imposed on the reconstructed invariant masses of the $\mathrm{W^+W^-}$, $m(\mathrm{W^+W^-}) > 2m_{\mathrm{W}}$, and neutrino pair, $m(\nu\bar{\nu}) > 0$.

To optimize the resolution of the ρ observable, an MVA approach is developed, based on a regression NN. Using the TensorFlow [87] package and the Keras [88] backend, a fully connected feed-forward NN is trained. An NN with two hidden layers of 512 nodes each is used. Low-level variables include basic event information such as the p_{T} of a reconstructed particle, whereas high-level variables include such things as the solutions to the kinematic reconstruction. Starting from a set of more than 100 low- and high-level input variables, the ten most relevant input variables are identified and selected, while the remaining ones are discarded. All events passing the selection described in Section 4 and having at least three reconstructed jets are considered in the training. As introduced in Section 3, a statistically independent training sample is obtained using $\mathrm{t\bar{t}}$ MC events simulated with the MadGraph5_aMC@NLO [FxFx] event generator interfaced with Pythia8. All NN hyperparameters are optimized using a Bayesian optimizer approach [89–91], and the final NN response is cross-checked using the POWHEG+Pythia8 simulation. Input variables, ordered by their impact, used for the regression NN are

- solution for ρ using the loose kinematic reconstruction,
- solution for ρ using the full kinematic reconstruction,
- invariant mass of the dilepton and subleading jet system,
- invariant mass of the leading lepton and subleading jet system,
- p_{T} of the subleading lepton,
- invariant mass of the dilepton,
- invariant mass of the subleading lepton and subleading jet system,
- invariant mass of the subleading lepton and leading jet system,
- invariant mass of the dilepton and leading jet system,

- $p_{\mathrm{T}}^{\mathrm{miss}}$.

If no solution from the kinematic reconstruction is obtained, a value of zero is used instead. The agreement between data and simulation for all inputs is evaluated using goodness-of-fit tests based on a saturated model [92]. All the input variables are found to have a p-value $>$ 0.08, when compared between data and simulation. The test procedure and the final result are independent of the cross section and not sensitive to m_{t}.

The performance of the NN regression is shown in Fig. 3, where the correlation between the parton-level ρ value (ρ_{true}) and the reconstructed value (ρ_{reco}) is shown. The regression correlation coefficient is 0.87, compared to 0.78 (0.84) for the loose (full) kinematic reconstruction. In the same figure, the ρ_{reco} resolution of the obtained solutions is displayed as a function of ρ_{true}. The ρ_{reco} resolution in each bin of ρ_{true} is defined as the root-mean-square of the difference between ρ_{reco} and ρ_{true}, divided by $1 + \langle \rho_{\mathrm{true}} - \rho_{\mathrm{reco}} \rangle$. A resolution between 0.05–0.08 is obtained over the entire spectrum, which is a significant improvement compared to the two analytical reconstruction methods that have a resolution in the range 0.10–0.13 for $\rho_{\mathrm{true}} > 0.5$. Moreover, unlike the kinematic reconstruction methods, which are affected by reconstruction inefficiencies, the NN approach gives a measurement of ρ for every event. In this analysis, the solution of the MVA regression is used, and is indicated with ρ_{reco}. Distributions of ρ_{reco} for the data and simulation are shown in Fig. 4 for the $\mathrm{e}^{\pm}\mu^{\mp}$ (left plot) and same-flavor (right plot) dilepton channels.

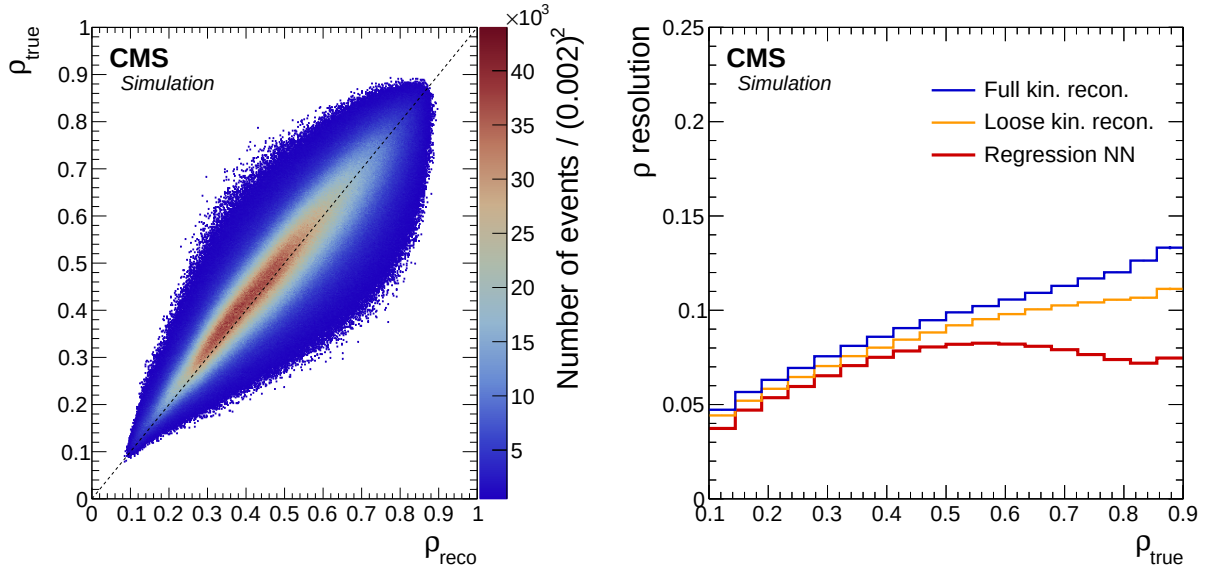

Figure 3: The correlation between ρ_{true} and ρ_{reco} is shown for the regression NN reconstruction method (left). The ρ_{reco} resolution, defined in the text, as a function of ρ_{true} (right) for the full (blue line) and loose (orange line) kinematic reconstructions and the regression NN (red line) methods. The number of events per bin in the left plot is shown by the color scale.

5.2 Event classification

To maximize the signal sensitivity and increase the separation between the $\mathrm{t\bar{t}}$+jet signal and Z+jets and $\mathrm{t\bar{t}}$+0 jet backgrounds, an MVA event classifier is developed. Using the same interface as for the regression NN, a fully connected feed-forward event-classification NN is defined, with the same strategies for the input-variable selection and optimization. Independent sets of training samples are obtained by using the NLO MADGRAPH5_aMC@NLO [FxFx]+PYTHIA8 simulation for the $\mathrm{t\bar{t}}$ and Z+jets events, which are not used in the likelihood

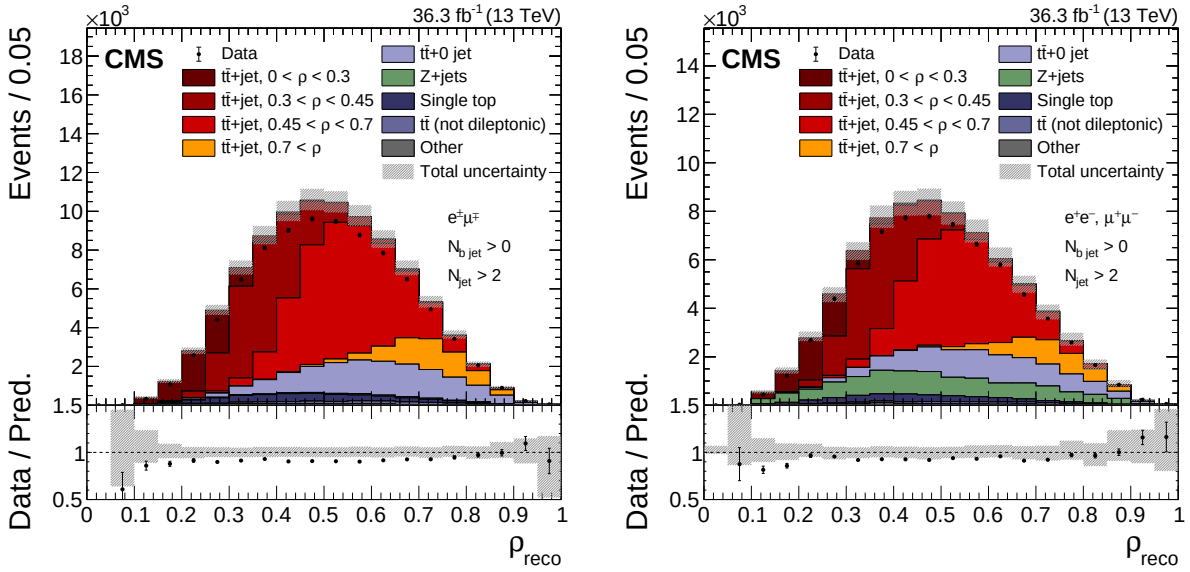

Figure 4: The observed (points) and MC predicted (stacked histograms) signal and background yields as a function of ρ_{reco} as determined by the NN reconstruction method for the $e^{\pm}\mu^{\mp}$ (left) and same-flavor dilepton channels (right). The vertical bars on the points represent the statistical uncertainty in the data. The hatched band represents the total uncertainty in the sum of the simulated signal and background predictions. The lower panels show the ratio of the data to the sum of the signal and background predictions.

fit. The input variables chosen for this NN, ranked by impact, are

- p_{T} of the additional third jet beyond the two jets from the top quark decays, as determined in the solution of the full kinematic reconstruction,
- p_{T} of the third-highest-p_{T} jet,
- invariant mass of the dilepton system,
- $p_{\text{T}}^{\text{miss}}$,
- mass of the leading lepton,
- mass of the subleading lepton,
- p_{T} of the leading jet,
- p_{T} of the dilepton system,
- number of reconstructed jets,
- p_{T} of the leading lepton.

The architecture of the classification network has three output nodes, corresponding to the three process classes ($\text{t}\bar{\text{t}}$+jet, Z+jets, and $\text{t}\bar{\text{t}}$+0 jet). The separation into multiple processes provides a better discrimination of the signal versus background events as compared to a binary-classifier approach. Because the response of the output nodes is used at a later step in the unfolding procedure (Section 6), any bias in the obtained response with respect to the ρ observable is reduced by making use of unsupervised domain adaptation by back propagation [93]. In this method, additional layers are added to the NN with the optimization target of regressing ρ_{reco} as an ancillary output node, whereas the sign of the gradient in the back-propagation algorithm is inverted such that the NN does not learn to use input information sensitive to ρ_{reco}. The trained NN uses four hidden layers with 204 nodes each. The background rejection of the event-classification NN is shown in Fig. 5 by the distributions of the NN output scores

for the $t\bar{t}$+jet signal $s(t\bar{t}\text{+jet})$ (left) and $t\bar{t}$+0 jet background $s(t\bar{t})$ (right) events from data and simulation.

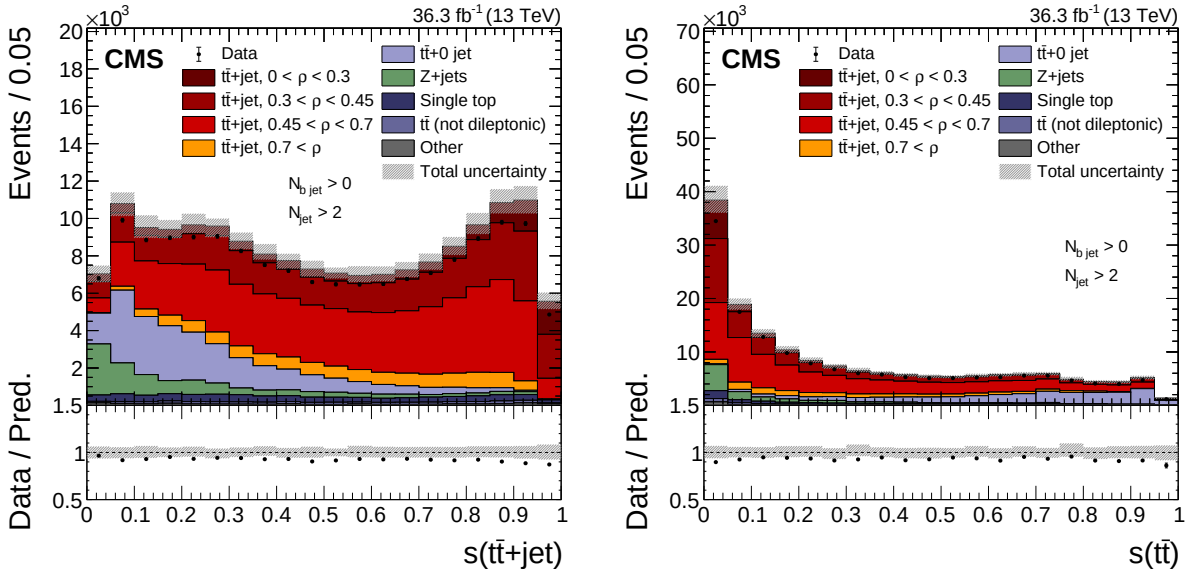

Figure 5: The observed (points) and MC predicted (stacked histograms) signal and background yields as a function of the signal (left) and $t\bar{t}$+0 jet background (right) output node score of the classifier NN. The vertical bars on the points represent the statistical uncertainty in the data. The hatched band represents the total uncertainty in the sum of the simulated signal and background predictions. The lower panels show the ratio of the data to the sum of the signal and background predictions.

6 Signal extraction, cross section measurement, and unfolding

The differential cross section $\mathrm{d}\sigma_{t\bar{t}\text{+jet}}/\mathrm{d}\rho$ is measured at the parton level in four ρ bins using a maximum likelihood fit to final-state distributions following the method of Ref. [32]. Systematic uncertainties are profiled in the likelihood function as nuisance parameters and are constrained using the data. The expected signal and background distributions and the effect of the systematic uncertainties are estimated using the MC simulations. The total cross section in each bin k of the ρ distribution, $\sigma^{k}_{t\bar{t}\text{+jet}}$, is measured. This is related to the differential cross section $\mathrm{d}\sigma_{t\bar{t}\text{+jet}}/\mathrm{d}\rho$ as

$$\sigma^{k}_{t\bar{t}\text{+jet}} = \int_{\rho^{k}_{\text{low}}}^{\rho^{k}_{\text{high}}} \frac{\mathrm{d}\sigma_{t\bar{t}\text{+jet}}}{\mathrm{d}\rho}\,\mathrm{d}\rho, \tag{2}$$

where ρ^{k}_{low} and ρ^{k}_{high} denote the lower and the upper bounds of the k-th generator-level bin in ρ, respectively.

The likelihood function $\mathcal{L}$ assumes that the number of observed events in each bin follows a Poisson distribution and can be written as:

$$\mathcal{L} = \prod_{i} \frac{\mathrm{e}^{-v_i} v_i^{n_i}}{n_i!} \prod_{j} \pi(w_j) \prod_{m} \pi(\lambda_m). \tag{3}$$

Here, i denotes the index of the bin in the final-state distribution, and v_i and n_i are the expected and observed number of events in bin i, respectively. The additional terms $\pi(w_j)$ and $\pi(\lambda_m)$

are the prior probability density functions (pdfs) for the normalization of each background process w_j and nuisance parameter λ_m, respectively.

The expected number of events v_i can be written as:

$$v_i = \sum_k s_i^k \left(\sigma^k_{\mathrm{t\bar{t}+jet}}, \vec{\lambda}, m_\mathrm{t}^\mathrm{MC}\right) + \sum_j b_i^j \left(w_j, \vec{\lambda}, m_\mathrm{t}^\mathrm{MC}\right), \tag{4}$$

where s_i^k is the number of expected $\mathrm{t\bar{t}}$+jet signal events from the k-th generator-level bin for a reconstructed ρ value in bin i. The value of s_i^k depends on $\sigma^k_{\mathrm{t\bar{t}+jet}}$, the nuisance parameters $\vec{\lambda}$, and the top quark mass used in the simulation m_t^MC, which is needed to model the acceptance and extrapolate the results to the full phase space. Analogously, b_i^j is the number of expected background events from process j, and depends on its normalization w_j, the nuisance parameters $\vec{\lambda}$, and on m_t^MC in the case of the $\mathrm{t\bar{t}}$ and tW backgrounds.

Since v_i implicitly incorporates the dependence of the parton-level cross section $\sigma^k_{\mathrm{t\bar{t}+jet}}$ on the experimental acceptance and detector response, the maximization of the likelihood function yields the results that are directly unfolded to the parton level.

For each cross section bin k, a signal strength parameter r_k is assigned, defined as

$$r_k = \frac{\sigma^k_{\mathrm{t\bar{t}+jet}}}{\sigma^k_{\mathrm{t\bar{t}+jet}}(\mathrm{MC})}, \tag{5}$$

where the denominator is the cross section corresponding to the normalization of the MC simulation. In the fit, all the signal strength parameters are fitted simultaneously. The $\sigma^k_{\mathrm{t\bar{t}+jet}}(\mathrm{MC})$ values are determined using the nominal NLO POWHEG+PYTHIA8 simulation, and the nuisance parameters are constrained simultaneously with the differential cross section values.

To mitigate the correlation between the fitted signal strength parameters and m_t^MC, the latter is added as an additional free parameter to the fit. For this purpose, additional predictions are obtained from two dedicated MC simulations where the value of m_t^MC is set to 169.5 or 175.5 GeV. In the simultaneous fit, the dependence of the measured $\sigma^k_{\mathrm{t\bar{t}+jet}}$ on m_t^MC is fully taken into account. Therefore, the resulting $\mathrm{d}\sigma_{\mathrm{t\bar{t}+jet}}/\mathrm{d}\rho$ can be compared to the fixed-order calculations without assumptions on the relationship between m_t^MC and $m_\mathrm{t}^\mathrm{pole}$ [94]. This method was proposed in Refs. [25, 94] and was used in previous CMS measurements [22, 32]. The likelihood construction and the minimization of $-2\ln(\mathcal{L})$ using MINUIT [95] follows the procedures described in Refs. [96–98], as does the estimation of the uncertainties using MINOS [95]. The nuisance parameters corresponding to the shape and normalization are modeled using Gaussian and log-normal prior pdfs, respectively, based on their input uncertainties before the fit to the data. The dependence of the templates on the nuisance parameters is interpolated quadratically (linearly) within (beyond) one standard deviation, as described in Ref. [99]. The systematic uncertainty templates are built so as to reflect the variations found in estimating the systematic uncertainties.

The measurement is performed in four bins of ρ_true and ρ_reco: 0–0.3, 0.3–0.45, 0.45–0.7, and 0.7–1.0, where the bin boundaries are determined by considering the experimental resolution and migration effects. The bin edges are chosen so that the purity and stability of each bin is $\geq$50%. The purity (stability) is defined as the number of signal events that are generated and reconstructed in the same bin, divided by the total number of signal events generated

(reconstructed) in that bin. The unfolding problem is determined to be well conditioned, and therefore no regularization is required.

6.1 Event categorization

The sensitivity of the cross section measurement to the different signal processes is enhanced by splitting the reconstructed events into multiple categories based on the jet ($N_{\text{jet}} = 1$, $N_{\text{jet}} = 2$, and $N_{\text{jet}} \geq 3$) and b jet multiplicities ($N_{\text{b jet}} = 1$ and $N_{\text{b jet}} \geq 2$) and the ρ_{reco} bin. The different event types are labeled as "mjnb" for events with m jets and n b jets. Events with fewer than three reconstructed jets, corresponding mainly to background $\mathrm{t\bar{t}}$+0 jet and Z+jets production, are also included in the fit. This maximizes the acceptance of the events reconstructed in the visible phase space and helps to constrain the background. Final-state distributions for each category are chosen that maximize the signal sensitivity. The relative signal response R_{NN} of the NN classifier, defined as: $R_{\text{NN}} = s(\mathrm{t\bar{t}}\text{+jet}) / [s(\mathrm{t\bar{t}}\text{+jet}) + s(\mathrm{t\bar{t}}\text{+0 jet})]$, is used as the observable for event categories with more than two reconstructed jets. To increase the fit sensitivity to $m_{\mathrm{t}}^{\text{MC}}$, the minimum invariant mass $m_{\ell\mathrm{b}}^{\text{min}}$ among the lepton and b jet combinations is used as the observable for events with two jets, where both are b tagged. In the remaining categories, the p_{T} of the lowest-p_{T} jet is fitted. The three dileptonic channels are kept separate in the fit and are treated as independent categories to disentangle the effects of systematic uncertainties in the different lepton flavors. An overview of the event categories and the chosen distributions are given in Table 1. Good agreement between the distributions from data and simulation is found.

Table 1: A list of the event categories and distributions used in the maximum likelihood fit.

	Reconstructed ρ				No reconstructed ρ	
	$N_{\text{jet}} \geq 3$				$N_{\text{jet}} = 1$	$N_{\text{jet}} = 2$
	$\rho < 0.3$	$0.3 < \rho < 0.45$	$0.45 < \rho < 0.7$	$\rho > 0.7$		
$N_{\text{b jet}} = 1$	R_{NN}	R_{NN}	R_{NN}	R_{NN}	$p_{\mathrm{T}}^{\text{leading jet}}$	$p_{\mathrm{T}}^{\text{subleading jet}}$
$N_{\text{b jet}} \geq 2$	R_{NN}	R_{NN}	R_{NN}	R_{NN}	—	$m_{\ell\mathrm{b}}^{\text{min}}$

In the binning of each observable, the statistical uncertainty in the nominal and systematic uncertainty templates is considered to reduce its impact on the extracted values of r_k, w_j, and $\vec{\lambda}$ after the fit to data. In particular, the kinematic distributions listed in Table 1 are reduced to the total event yield if the number of simulated events is insufficient to model the kinematic distributions properly. As a criterion, the statistical uncertainty in the number of simulated events is not allowed to exceed 0.5% per bin. The final input distributions to the fit are displayed in Fig. 6, where the data are compared to the simulated signal and background distributions before the fit.

7 Systematic uncertainties

Contributions to the systematic uncertainties from various sources are modeled as nuisance parameters in the fit, as described in Section 6. For each variation, dedicated templates are obtained describing the effect on each background source or signal contribution.

7.1 Experimental uncertainties

Most of the experimental systematic uncertainties are estimated by varying the scale factors (SFs) used to correct any differences between the data and simulation. The following experimental uncertainties are considered:

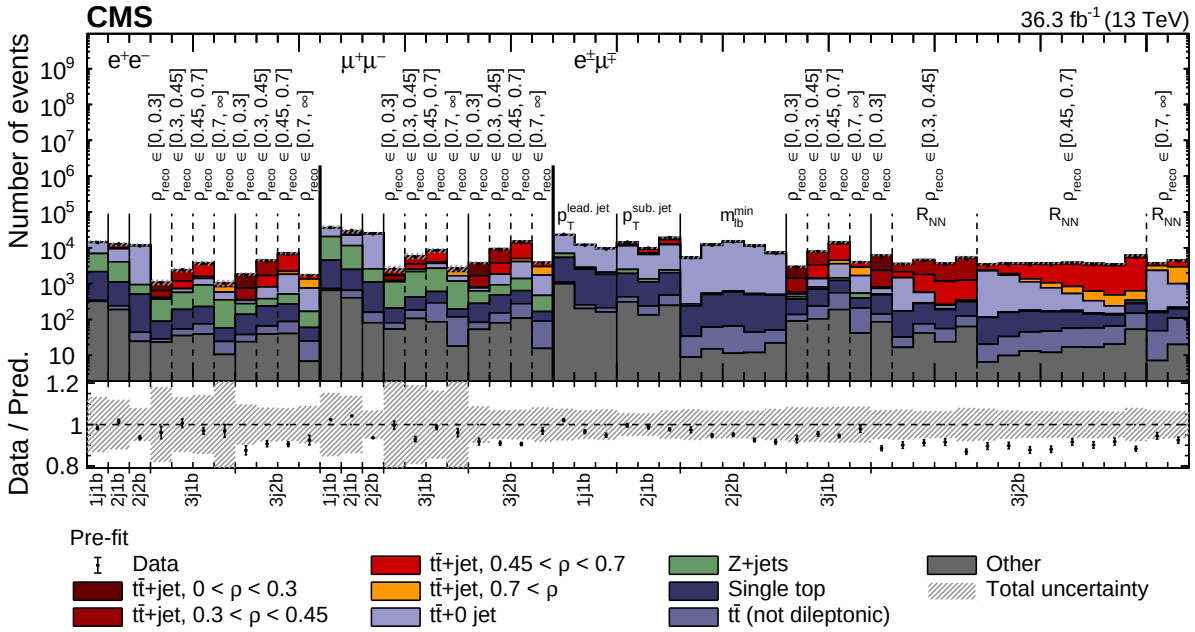

Figure 6: The distributions from data (points) and simulated signal and background (colored histograms) used in the maximum likelihood fits before the fit to the data. The distributions are shown for each dilepton type and each event category, where the x-axis label "mjnb" refers to events with m jets and n b jets. The vertical bars on the points show the statistical uncertainty in the data. The hatched band represents the total uncertainty in the sum of the simulated signal and background predictions. The lower panel gives the ratio of the data to the sum of the simulated predictions.

- The integrated luminosity used to normalize the simulated samples has a relative uncertainty of 1.2% [100].
- The uncertainty in the amount of pileup is estimated by varying the total inelastic pp cross section by its measurement uncertainty of 4.6% [77] in the simulation.
- To correct for differences in the trigger efficiencies between data and simulation, dedicated SFs are derived in p_{T} and η bins of the leading and subleading leptons. These SFs are typically close to unity and are varied within their uncertainties, which are composed of statistical and systematic components are smaller than 3%.
- Electron and muon identification and isolation efficiencies are measured in bins of the lepton p_{T} and η [47, 48]. Corresponding SFs are consistent with unity within 10 and 3% for electrons and muons, respectively. They are varied within their uncertainties in the simulation to estimate the corresponding systematic uncertainty.
- Uncertainties due to correcting the electron and muon energy scales and resolutions are assessed separately by varying them within their uncertainties in the simulation. The typical energy resolution is on the order of 2–5 and 1–3% for electrons and muons, respectively [47, 48]. The energy variations are propagated to $\vec{p}_{\mathrm{T}}^{\,\mathrm{miss}}$.
- Several uncertainties affecting the correction of the jet energy scale (JES) are split into a set of 23 individual contributions [42]. They are varied as a function of the jet p_{T} and η, and the effect is propagated to $\vec{p}_{\mathrm{T}}^{\,\mathrm{miss}}$. The total uncertainty in the JES ranges from 1.0–3.5% depending on the jet kinematic variables [42].
- An additional uncertainty in $\vec{p}_{\mathrm{T}}^{\,\mathrm{miss}}$ is derived by varying the energies of reconstructed particles not clustered into jets. Its effect on the resolution is on the order of 5–

30% [101].

- The effect from the jet energy resolution (JER) is estimated by varying the SFs for the jet four-momenta within their uncertainty on the order of 2–8%, depending on the η region [42].
- Uncertainties in the correction of the simulation coming from the application of the pileup jet identification are estimated by varying the efficiency and mistagging rate within their uncertainties [45, 102]. The agreement between the data and simulated samples is in the range of 2–10% [45], depending on the jet η and p_{T}.
- During the 2016 data taking, a gradual shift in the timing of the inputs to the ECAL L1 trigger in the region $|\eta| > 2.0$ caused a specific trigger inefficiency. For events containing an electron (jet) with p_{T} larger than ≈50 (100) GeV, in the region $2.5 < |\eta| < 3.0$ the efficiency loss is ≈10–20%, depending on p_{T}, η, and the data-taking period [37]. A similar effect was present for L1-trigger muons because of the finite time resolution of the muon detectors, leading to an effect of 0.5–1.5% per muon [103]. Dedicated SFs are derived for correcting the simulation for this effect known as "prefiring" and are varied within their uncertainties.
- To correct for different b tagging efficiencies and mistagging rates of light-quark and gluon jets in the data and simulation, SFs are derived using simulated QCD multijet events and are applied as a function of the jet p_{T} [80]. To estimate the impact of that systematic uncertainty, the SFs are varied within their estimated uncertainties, which are split into individual subsources. For light- and heavy-quark jets the uncertainty ranges from 5-10 and 1-5%, respectively.

7.2 Theoretical uncertainties

Additional systematic uncertainties arise from assumptions on the model parameters of the nominal POWHEG+PYTHIA8 simulation. Their effect is estimated by appropriate variations in the simulated samples. The following theoretical uncertainties are considered:

- To estimate the effect of missing higher-order corrections in the NLO simulation, the μ_{R} and μ_{F} scales are varied by a factor of two up and down in the POWHEG calculation with respect to their nominal values. Combined variations of μ_{R} and μ_{F} are not considered.
- Uncertainties in the modeling of the parton shower are assessed by varying individually the corresponding scales for the initial- (ISR) and final-state radiation (FSR) by a factor of two up and down with respect to their nominal values.
- The PDF uncertainty is estimated by using the 100 eigenvector variations of the NNPDF3.1 PDF set [52, 53], each treated as an individual nuisance parameter in the fit. Additionally, the value of $\alpha_{\mathrm{S}}(m_{\mathrm{Z}})$, where m_{Z} is the Z boson mass, is varied within its uncertainty in this PDF set.
- The dependence on the matching between the ME and PS generators is estimated by varying the h_{damp} parameter in the POWHEG simulation within the tuning uncertainties [55] in dedicated simulated samples.
- The modeling dependence on the CP5 UE tune is evaluated by varying the tune parameters within their uncertainties [55], for which dedicated samples are generated.
- In the PYTHIA8 setup used for the nominal simulation, certain assumptions are made on the modeling of color reconnection (CR). While early-resonance decays (ERD) are turned off in the nominal setting, a dedicated sample with ERD enabled is generated,

and the difference is treated as a systematic uncertainty. Moreover, alternative CR models are considered, including a gluon-move scheme [104] and a QCD-inspired scheme [105].

- Uncertainties originating from the limited knowledge of the b hadron fragmentation function are estimated by varying the parameters of the Bowler–Lund function within their uncertainties [106]. Alternatively, the Peterson fragmentation function [107] is used.
- The limited precision on the semileptonic branching fractions of b hadrons is estimated by varying them within their uncertainties, as estimated in Ref. [4].

Besides the PDF and h_{damp} variations, all the above-mentioned uncertainties are also assessed for tW production and are considered correlated, if applicable. In the case of Z+jets production, μ_{R} and μ_{F} variations are also considered. The theoretical uncertainties in the extrapolation to the full phase space are estimated by evaluating their impact on the signal acceptance. In this procedure we ignore possible post-fit constraints on these sources of uncertainties, obtained from events reconstructed in the visible phase space [22, 32].

7.3 Additional uncertainties

Additional uncertainties arise from the normalizations of the background processes, the finite number of events in the MC simulation, and the corresponding effects on the templates from these sources.

The uncertainties in the normalizations for single top quark production and smaller background contributions, such as diboson and W+jets production, are taken to be 30% and modeled with a log-normal prior pdf, following the prescriptions from previous analyses [22, 29, 85]. For the Z+jets background, separate uncertainties are used for each b jet category in order to remove the dependence of the fit result on the prediction of the b jet multiplicity distribution from the Z+jets simulation. Similarly, the Z+jets background is assigned an additional uncertainty of 5, 10, 30, and 50% for events with exactly 0, 1, 2, and 3 or more jets, respectively. The first three uncertainties are estimated by performing scale variations in the W+jets predictions with NLO precision, whereas the last one is assigned conservatively [22]. For the $\mathrm{t\bar{t}}$+0 jet background, no prior pdf is used since the normalization is left free in the fit in order to help constrain it with the background-dominated categories.

The statistical uncertainty due to the finite size of the MC event samples is evaluated via bin-by-bin nuisance parameters with the Barlow–Beeston "light" method [99, 108]. In addition, the impact of the finite statistical precision on the predictions of the MC samples with dedicated systematic variations is cross-checked using toy experiments, following the approach described in Ref. [32], and was found to be negligible.

8 Results and extraction of the top quark mass

Figure 7 compares the resulting data distributions after the fit to the MC signal and background predictions. The measured absolute differential cross section $\mathrm{d}\sigma_{\mathrm{t\bar{t}+jet}}/\mathrm{d}\rho$ is shown in Fig. 8 (left) and compared to the NLO QCD predictions. The latter are obtained using the $\mathrm{t\bar{t}}$+jet process implemented in POWHEG-BOX [109], with the ABMP16NLO [110] PDF set, and assuming $m_{\mathrm{t}}^{\text{pole}}$ values of 169.5, 172.5, and 175.5 GeV. It is worth mentioning that in the ABMP analysis, the PDFs and $\alpha_{\mathrm{S}}(m_{\mathrm{Z}})$ are obtained simultaneously at the same perturbative order in QCD. Additionally, the CT18NLO PDF set [111] is considered.

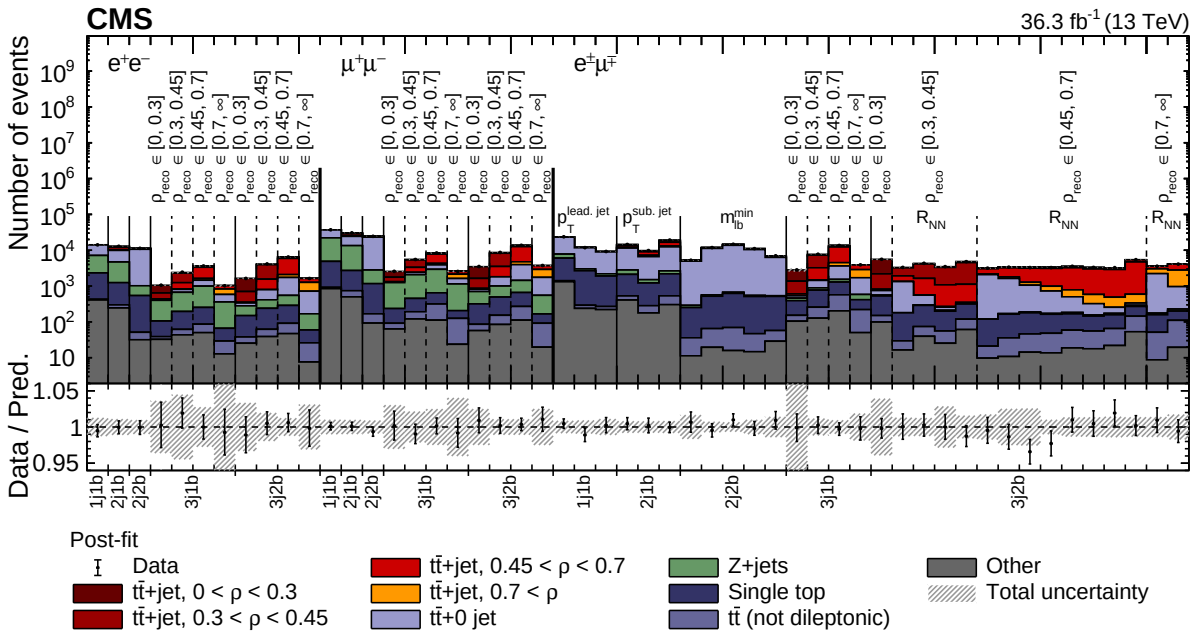

Figure 7: The distributions from data (points) and simulated signal and background (colored histograms) used in the maximum likelihood fits after the fit to the data. The distributions are shown for each dilepton type and each event category, where the x-axis label "*mjn*b" refers to events with *m* jets and *n* b jets. The vertical bars on the points show the statistical uncertainty in the data. The hatched band represents the total uncertainty in the sum of the simulated signal and background predictions. The lower panel gives the ratio of the data to the sum of the simulated predictions.

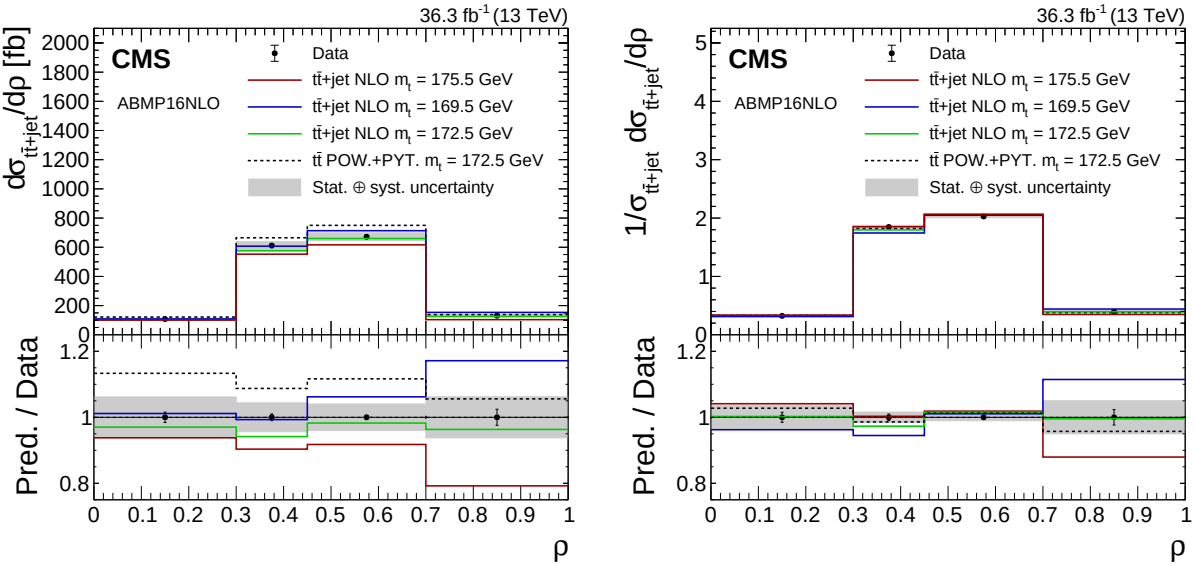

Figure 8: The absolute (left) and normalized (right) $t\bar{t}$+jet differential cross section as a function of ρ for the data (points) and theoretical predictions described in the text using the AMBP16NLO PDF set from the NLO MC with three different m_t values and from the POWHEG (POW) + PYTHIA8 (PYT) calculations (lines). The vertical bars on the points show the statistical uncertainty in the data and the shaded region represents the total uncertainty in the measurement. The lower panels give the ratio of the predictions to the data.

The QCD scale in the theoretical prediction is dynamically set to $H_{\mathrm{T}}^{B}/2$, as suggested in Ref. [112] and discussed in Ref. [113], where H_{T}^{B} is defined as the scalar sum of the top quark and antiquark transverse masses and the p_{T} of the additional jet. The values and the uncertainty in the normalized differential cross section are derived from the fit results for the absolute cross section by taking into account the covariance matrix as obtained in the fit to data. The normalized differential cross section is determined by dividing the value of the absolute differential cross section for each bin by the sum of the values of all the bins. Uncertainties are symmetrized prior to the normalization as provided by HESSE [95]. The results are shown in Fig. 8 (right) in comparison with the theoretical predictions. While the absolute cross section shows a stronger dependence on α_{S}, this dependence is small for the normalized cross section [113]. All the sources and values of the systematic uncertainties in the differential cross section result are given in Table 2.

The fitted parameter values, expected and observed constraints, and impacts on the signal strengths r_k for the 30 most important nuisance parameters after the fit to data are shown in Fig. 9. For each parameter, the difference between the best fit ($\hat{\theta}$) and input value (θ_0) is given relative to the input uncertainty $\Delta\theta$, while the constraint is defined as the uncertainty after the fit relative to the input uncertainty. For the nuisance parameters associated with the $\mathrm{t\bar{t}}$+0 jet normalization and $m_{\mathrm{t}}^{\mathrm{MC}}$, the values of the nuisance parameters after the fit are given in the figure instead of plotting $(\hat{\theta}-\theta_0)/\Delta\theta$ theta because no prior pdf is assigned. The values of the nuisance parameters after the fit are compatible with the corresponding values before the fit within their prior uncertainties, reflecting the good agreement between data and simulation before the fit. Some differences between $\hat{\theta}$ and θ_0 for nuisance parameters describing the background normalization for the single top quark and Z+jets processes are larger. This is expected because of the limitations in the MC simulations used to model these backgrounds in the signal phase space region, which corresponds to the corners of the background phase space. The nuisance parameter associated with the modeling of the top quark p_{T} spectra also has a larger value after the fit. This is because of the different spectra observed in data and simulation, as discussed in Section 4.

The observed constraints and impacts agree with the expectations derived from fitting pseudo-data obtained from the nominal simulation. Strong constraints are determined on the normalizations of the background Z+jets and single top quark processes, which are explained by their large number of events in the background-dominated categories that helps to constrain the large normalization uncertainty. The nuisance parameter associated with the electron identification efficiency has a tight constraint from combining decay channels with different electron and muon multiplicities in the fit. This effect was seen in previous CMS measurements [22, 32].

The constraints on nuisance parameters associated with the jet energy corrections, JER, and jet identification demonstrate the power of the fit method, since the analysis phase space region and fitted kinematic distributions are sensitive to these effects. Also, because the analyzed phase space region is different from the one used to derive the corresponding calibrations described in Section 7, deviations from the values before the fit and constraints are expected. In the fit, $m_{\mathrm{t}}^{\mathrm{MC}}$ is determined as $171.93 \pm 0.65\,\mathrm{GeV}$, where the uncertainty includes both the statistical and systematic components.

The value of $m_{\mathrm{t}}^{\mathrm{pole}}$ is extracted from a χ^2 fit of the normalized differential cross section to the NLO theoretical predictions for the cross section. Since in a fit to a normalized distribution, the value of any bin is fully determined by the value of the others, one bin is removed from the χ^2 fit. The result is independent of the choice of the removed bin. The PDF uncertainties are evaluated in each bin and included in the total covariance matrix. For CT18NLO, the un-

Table 2: The relative uncertainties $\Delta\sigma^{k}_{\mathrm{t\bar{t}+jet}}$ in the parton-level cross section values $\sigma^{k}_{\mathrm{t\bar{t}+jet}}$ and their sources in each bin k of the ρ distribution. The statistical uncertainty is evaluated by keeping all nuisance parameters fixed to their values after the fit to data. The breakdown of the uncertainty is obtained by repeating the fit after fixing all but the nuisance parameters related to the components under consideration to their fitted values. The partial uncertainty is then estimated by subtracting the statistical component from the total uncertainty obtained with this procedure. The quadratic sum of the contributions is different from the total uncertainty because of correlations between the nuisance parameters.

Uncertainty Source	$\Delta\sigma^{1}_{\mathrm{t\bar{t}+jet}}$ [%]	$\Delta\sigma^{2}_{\mathrm{t\bar{t}+jet}}$ [%]	$\Delta\sigma^{3}_{\mathrm{t\bar{t}+jet}}$ [%]	$\Delta\sigma^{4}_{\mathrm{t\bar{t}+jet}}$ [%]
Experimental				
Muon identification	0.3	0.2	0.2	0.5
Muon energy scale and resolution	0.2	$\leq$0.1	$\leq$0.1	0.2
Electron identification	0.3	0.2	0.2	0.5
Electron energy scale and resolution	0.1	$\leq$0.1	0.1	0.3
Jet energy scale	1.0	0.5	0.5	1.3
Jet energy resolution	0.3	0.3	0.5	0.2
Jet identification	0.2	0.4	0.4	1.1
$p_{\mathrm{T}}^{\mathrm{miss}}$	$\leq$0.1	$\leq$0.1	$\leq$0.1	$\leq$0.1
b jet identification	0.3	0.1	0.1	0.2
Trigger efficiency	0.3	0.3	0.3	0.6
Total	2.1	1.6	1.7	2.9
Background normalization				
$\mathrm{t\bar{t}}$+0 jet	$\leq$0.1	0.1	0.1	0.4
Z+jets	0.4	0.2	0.2	0.6
Single top quark	0.2	0.1	0.1	0.2
Total	0.8	0.4	0.3	0.7
Modeling				
Z+jets ME scale	0.2	0.1	0.1	0.3
Single top quark ME/FSR/ISR scales	1.0	0.2	0.1	0.2
$\mathrm{t\bar{t}}$ PDF	0.1	$\leq$0.1	$\leq$0.1	0.1
$\mathrm{t\bar{t}}$ ME scale	0.7	0.1	0.2	0.6
$\mathrm{t\bar{t}}$ ISR scale	0.1	0.1	0.1	0.1
$\mathrm{t\bar{t}}$ FSR scale	0.2	0.2	0.3	0.4
$\mathrm{t\bar{t}}$ top quark p_{T}	0.7	0.5	0.2	0.6
b fragmentation	0.2	0.1	0.2	0.2
Color reconnection	0.2	$\leq$0.1	0.2	$\leq$0.1
$\mathrm{t\bar{t}}$ matching scale	0.1	0.2	$\leq$0.1	0.1
Underlying-event tune	0.1	$\leq$0.1	0.1	$\leq$0.1
Total	1.8	0.8	0.5	1.2
Integrated luminosity	0.3	0.3	0.3	0.6
$m_{\mathrm{t}}^{\mathrm{MC}}$	0.1	$\leq$0.1	0.3	0.1
Finite size of simulated samples	1.1	0.5	0.4	1.5
Total systematic	6.0	4.3	4.0	5.7
Statistical	1.6	1.0	0.8	2.4
Total	6.2	4.4	4.0	6.2

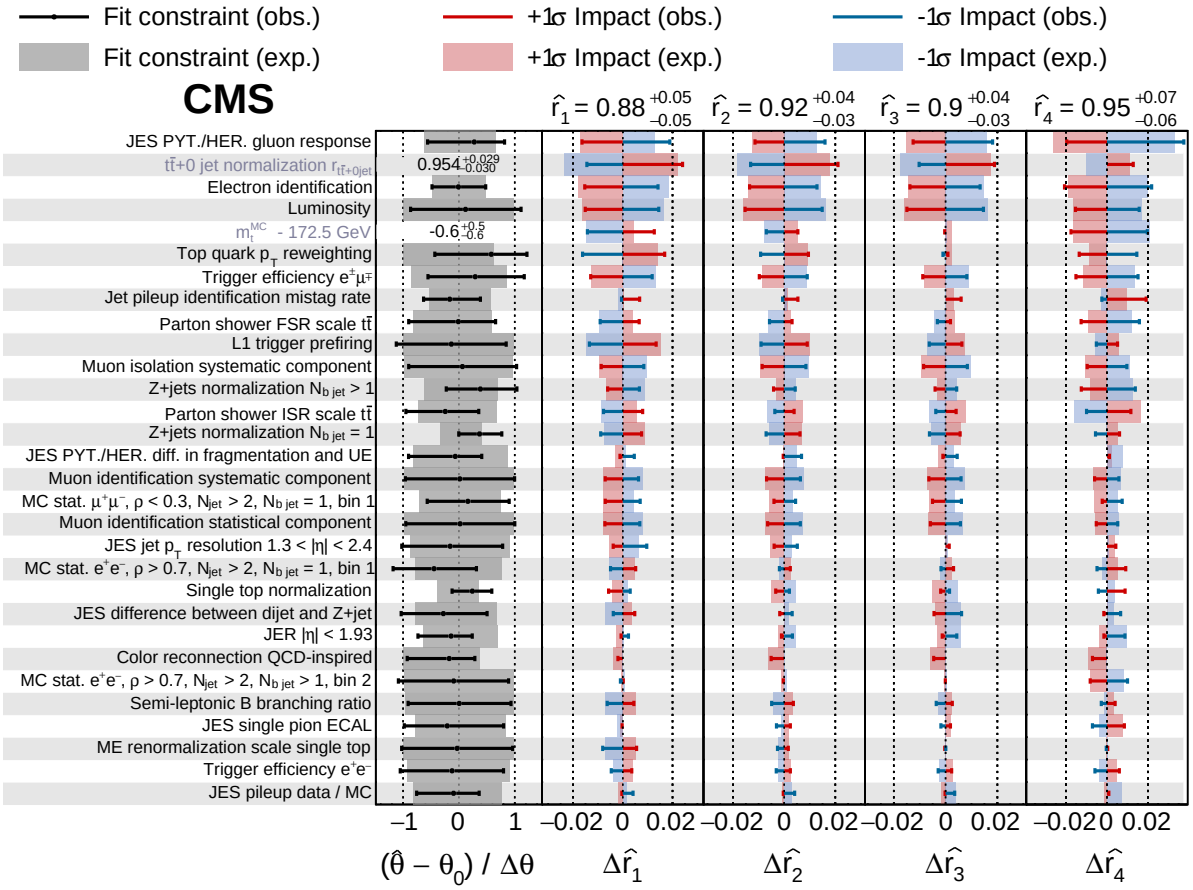

Figure 9: The fitted nuisance-parameter values and their impacts $\Delta\hat{r}_k$ on the signal strengths $\hat{r}_k$ from the fit to the data, ordered by their relative summed impact. Only the 30 highest ranked parameters are shown. The resulting fitted values of $\hat{r}_k$ and their total uncertainties are also given. The nuisance-parameter values ($\hat{\theta}$, black lines) are shown in comparison to their input values θ_0 before the fit and relative to their uncertainty $\Delta\theta$. The impact $\Delta\hat{r}_k$ for each nuisance parameter is the difference between the nominal best fit value of r_k and the best fit value when only that nuisance parameter is set to its best fit value $\hat{\theta}$ while all others are left free. The red and blue lines correspond to the variation in $\Delta\hat{r}_k$ when the nuisance parameter is varied up and down by its fitted uncertainty ($\Delta\theta$), respectively. The corresponding gray, red, and blue regions show the expected values from fits to pseudo-data. For the nuisance parameters associated with the $t\bar{t}$+0 jet normalization and m_t^{MC}, the values after the fit to the data are given, because no prior pdf is assigned.

certainties evaluated at 90% confidence level (CL), are rescaled to the 68% CL for consistency with the ABMP16NLO PDF set and symmetrized by taking the maximum of the up and down variation. Additionally, extrapolation uncertainties for all relevant theoretical uncertainties, as described in Section 7, are symmetrized by taking the average of the positive and negative impacts and are included in the calculation of the χ^2. The resulting χ^2 curves are shown in Fig. 10 (left). The best fit value for m_t^{pole} is extracted at the χ^2 minimum and the experimental uncertainty is obtained using the tolerance criterion of $\Delta\chi^2 = 1$.

To estimate the scale variation uncertainty, the fit is repeated using the theoretical predictions, with μ_R and μ_F varied independently by factors of 0.5 and 2, avoiding cases where $\mu_F/\mu_R = 4$ or $1/4$. The total scale uncertainty is estimated by taking the maximum difference in the results

to the nominal one. The resulting value of

$$m_t^{pole} = 172.94 \pm 1.27\,(\text{fit})\,^{+0.51}_{-0.43}\,(\text{scale})\,\text{GeV}$$

is obtained using the ABMP16NLO PDF set. The first uncertainty corresponds to the total statistical and systematic uncertainties from the fit including the PDF and extrapolation uncertainties, and the second uncertainty comes from the variation in the μ_R and μ_F scales. Using the CT18NLO PDF set instead, the measured value is

$$m_t^{pole} = 172.16 \pm 1.35\,(\text{fit})\,^{+0.50}_{-0.40}\,(\text{scale})\,\text{GeV}.$$

The total uncertainty in m_t^{pole} corresponds to 1.37 (1.44) GeV for the ABMP16NLO (CT18NLO) PDF set. Comparisons between the unfolded data and theoretical predictions for the determined values of m_t^{pole} with both PDF sets are given in Fig. 10 (right), showing good agreement between the fitted prediction and the measured cross section for both PDF sets.

The obtained results are in good agreement with previous measurements of m_t^{pole} using $t\bar{t}$+jet events [35] at a center-of-mass energy of 8 TeV by ATLAS and the triple-differential cross sections for $t\bar{t}$ production at a center-of-mass energy of 13 TeV by CMS [29]. Compared to the ATLAS result, a lower sensitivity to m_t^{pole} is expected in this analysis due to the higher center-of-mass energy. Furthermore, in this analysis the systematic uncertainty due to the PDFs is fully taken into account, which leads to an increase in the total uncertainty in m_t^{pole}.

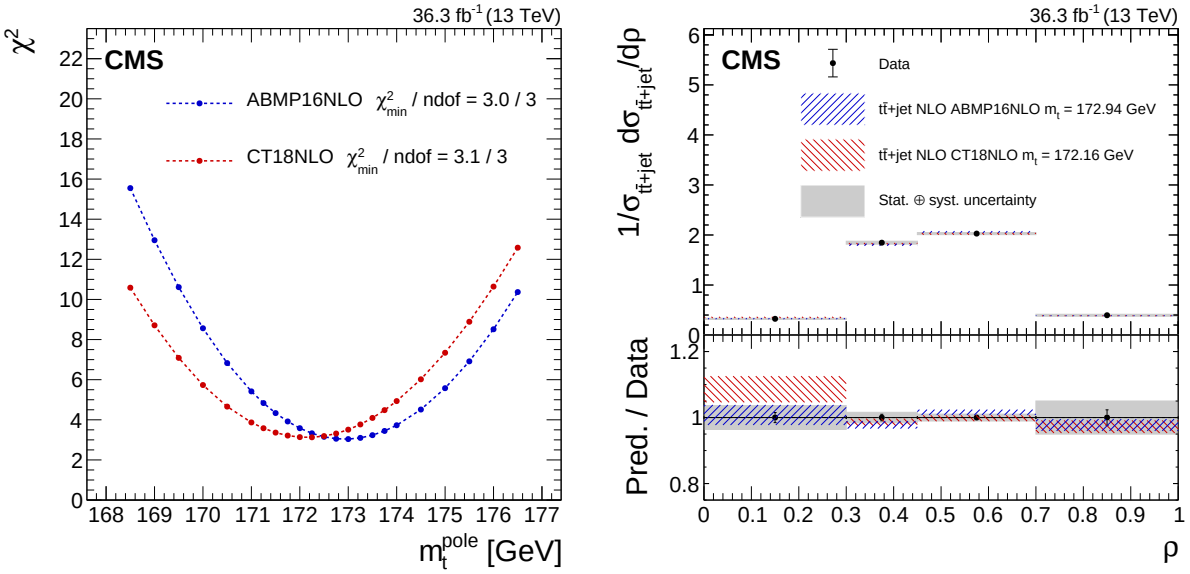

Figure 10: Left: The χ^2 values versus m_t^{pole} from the fit of the measured normalized $t\bar{t}$+jet differential cross sections to the theoretical predictions using the ABMP16NLO (blue points) and CT18NLO (red points) PDF sets. The minimum χ^2 value and the number of degrees of freedom (ndof) are given for each fit. Right: The measured normalized $t\bar{t}$+jet differential cross section (points) as a function of ρ, compared to the predictions using the two PDF sets and the corresponding best fit values for m_t^{pole} (hatched bands). The lower panel gives the ratio of the theoretical predictions to the measured values. For both panels, the vertical bars on the points show the statistical uncertainty in the data, the height of the hatched bands represent the theoretical uncertainties in the predictions, and the gray band gives the total uncertainty in the measured cross section.

9 Summary

Measurements are presented of the normalized differential cross section of top quark-antiquark pair ($\mathrm{t\bar{t}}$) production in association with at least one additional jet as a function of the inverse of the invariant mass of the $\mathrm{t\bar{t}}$+jet system $\rho = 2m_0/m_{\mathrm{t\bar{t}+jet}}$, with the scaling constant $m_0 = 170\,\mathrm{GeV}$. Proton-proton collision data collected by the CMS experiment at the CERN LHC at a center-of-mass energy of 13 TeV are used, corresponding to an integrated luminosity of $36.3\,\mathrm{fb}^{-1}$. Events in the dilepton decay channel are considered, and a novel multivariate analysis technique is applied to maximize the sensitivity to the signal process. The differential cross section is measured at the parton level using a maximum likelihood fit to final-state observables, where all systematic uncertainties are profiled. The value of the top quark pole mass $m_{\mathrm{t}}^{\mathrm{pole}}$ is extracted by comparing the measured $\mathrm{t\bar{t}}$+jet normalized differential cross section as a function of ρ to theoretical predictions at next-to-leading order in quantum chromodynamics, obtained with two sets of parton distribution functions. The $m_{\mathrm{t}}^{\mathrm{pole}}$ values is determined to be $172.94 \pm 1.37\,\mathrm{GeV}$ and $172.16 \pm 1.44\,\mathrm{GeV}$ using the ABMP16NLO and CT18NLO parton distribution functions, respectively. Here, the uncertainties shown include the total statistical and systematic uncertainties including extrapolation uncertainties, and the theoretical uncertainties from the parton distribution functions and the matrix-element scales. The results are in good agreement with previous measurements.

References

[1] Gfitter Group Collaboration, "The global electroweak fit at NNLO and prospects for the LHC and ILC", *Eur. Phys. J. C* **74** (2014) 3046, doi:10.1140/epjc/s10052-014-3046-5, arXiv:1407.3792.

[2] J. de Blas et al., "Electroweak precision observables and Higgs-boson signal strengths in the standard model and beyond: present and future", *JHEP* **12** (2016) 135, doi:10.1007/JHEP12(2016)135, arXiv:1608.01509.

[3] S. Alekhin, J. Blümlein, S. Moch, and R. Placakyte, "Parton distribution functions, α_{S}, and heavy-quark masses for LHC Run II", *Phys. Rev. D* **96** (2017) 014011, doi:10.1103/PhysRevD.96.014011, arXiv:1701.05838.

[4] Particle Data Group, P. A. Zyla et al., "Review of particle physics", *Prog. Theor. Exp. Phys.* **2020** (2020) 083C01, doi:10.1093/ptep/ptaa104.

[5] G. Degrassi et al., "Higgs mass and vacuum stability in the standard model at NNLO", *JHEP* **08** (2012) 098, doi:10.1007/JHEP08(2012)098, arXiv:1205.6497.

[6] S. Alekhin, A. Djouadi, and S. Moch, "The top quark and Higgs boson masses and the stability of the electroweak vacuum", *Phys. Lett. B* **716** (2012) 214, doi:10.1016/j.physletb.2012.08.024, arXiv:1207.0980.

[7] ATLAS Collaboration, "Measurement of the top quark mass in the $\mathrm{t\bar{t}} \to$ dilepton channel from $\sqrt{s} = 8\,\mathrm{TeV}$ ATLAS data", *Phys. Lett. B* **761** (2016) 350, doi:10.1016/j.physletb.2016.08.042, arXiv:1606.02179.

[8] ATLAS Collaboration, "Top-quark mass measurement in the all-hadronic $\mathrm{t\bar{t}}$ decay channel at $\sqrt{s} = 8\,\mathrm{TeV}$ with the ATLAS detector", *JHEP* **09** (2017) 118, doi:10.1007/JHEP09(2017)118, arXiv:1702.07546.

[9] ATLAS Collaboration, "Measurement of the top quark mass in the $\mathrm{t\bar{t}} \to$ lepton+jets channel from $\sqrt{s} = 8$ TeV ATLAS data and combination with previous results", *Eur. Phys. J. C* **79** (2019) 290, doi:10.1140/epjc/s10052-019-6757-9, arXiv:1810.01772.

[10] CMS Collaboration, "Measurement of the top quark mass using proton-proton data at $\sqrt{s} = 7$ and 8 TeV", *Phys. Rev. D* **93** (2016) 072004, doi:10.1103/PhysRevD.93.072004, arXiv:1509.04044.

[11] CMS Collaboration, "Measurement of the top quark mass in the dileptonic $\mathrm{t\bar{t}}$ decay channel using the mass observables $m_{\mathrm{b}\ell}$, m_{T2}, and $m_{\mathrm{b}\ell\nu}$ in pp collisions at $\sqrt{s} = 8$ TeV", *Phys. Rev. D* **96** (2017) 032002, doi:10.1103/PhysRevD.96.032002, arXiv:1704.06142.

[12] CMS Collaboration, "Measurement of the top quark mass with lepton+jets final states using pp collisions at $\sqrt{s} = 13$ TeV", *Eur. Phys. J. C* **78** (2018) 891, doi:10.1140/epjc/s10052-018-6332-9, arXiv:1805.01428.

[13] CMS Collaboration, "Measurement of the top quark mass in the all-jets final state at $\sqrt{s} = 13$ TeV and combination with the lepton+jets channel", *Eur. Phys. J. C* **79** (2019) 313, doi:10.1140/epjc/s10052-019-6788-2, arXiv:1812.10534.

[14] CMS Collaboration, "Measurement of the top quark mass using events with a single reconstructed top quark in pp collisions at $\sqrt{s} = 13$ TeV", *JHEP* **12** (2021) 161, doi:10.1007/JHEP12(2021)161, arXiv:2108.10407.

[15] S. Ferrario Ravasio, T. Ježo, P. Nason, and C. Oleari, "A theoretical study of top-mass measurements at the LHC using NLO+PS generators of increasing accuracy", *Eur. Phys. J. C* **78** (2018) 458, doi:10.1140/epjc/s10052-018-5909-7, arXiv:1906.09166. [Addendum: doi:10.1140/epjc/s10052-019-7336-9].

[16] M. Butenschoen et al., "Top quark mass calibration for Monte Carlo event generators", *Phys. Rev. Lett.* **117** (2016) 232001, doi:10.1103/PhysRevLett.117.232001, arXiv:1608.01318.

[17] ATLAS, CDF, CMS, and D0 Collaborations, "First combination of Tevatron and LHC measurements of the top-quark mass", 2014. arXiv:1403.4427.

[18] S. Moch et al., "High precision fundamental constants at the TeV scale", 2014. arXiv:1405.4781.

[19] A. Juste et al., "Determination of the top quark mass circa 2013: methods, subtleties, perspectives", *Eur. Phys. J. C* **74** (2014) 3119, doi:10.1140/epjc/s10052-014-3119-5, arXiv:1310.0799.

[20] A. H. Hoang, "What is the top quark mass?", *Ann. Rev. Nucl. Part. Sci.* **70** (2020) 225, doi:10.1146/annurev-nucl-101918-023530, arXiv:2004.12915.

[21] A. H. Hoang, "The top mass: interpretation and theoretical uncertainties", in *Proc. 7th Int. Workshop on Top Quark Physics (TOP2014): Cannes, France, September 28–October 3, 2014*. 2014. arXiv:1412.3649.

[22] CMS Collaboration, "Measurement of the $\mathrm{t\bar{t}}$ production cross section, the top quark mass, and the strong coupling constant using dilepton events in pp collisions at $\sqrt{s} = 13\,\text{TeV}$", *Eur. Phys. J. C* **79** (2019) 368, doi:10.1140/epjc/s10052-019-6863-8, arXiv:1812.10505.

[23] ATLAS Collaboration, "Measurement of the $\mathrm{t\bar{t}}$ production cross-section using $\mathrm{e}\mu$ events with b-tagged jets in pp collisions at $\sqrt{s} = 7$ and 8 TeV with the ATLAS detector", *Eur. Phys. J. C* **74** (2014) 3109, doi:10.1140/epjc/s10052-014-3109-7, arXiv:1406.5375. [Addendum: doi:10.1140/epjc/s10052-016-4501-2].

[24] CMS Collaboration, "Measurement of the $\mathrm{t\bar{t}}$ production cross section in the $\mathrm{e}\mu$ channel in proton-proton collisions at $\sqrt{s} = 7$ and 8 TeV", *JHEP* **08** (2016) 029, doi:10.1007/JHEP08(2016)029, arXiv:1603.02303.

[25] CMS Collaboration, "Measurement of the $\mathrm{t\bar{t}}$ production cross section using events with one lepton and at least one jet in pp collisions at $\sqrt{s} = 13\,\text{TeV}$", *JHEP* **09** (2017) 051, doi:10.1007/JHEP09(2017)051, arXiv:1701.06228.

[26] ATLAS Collaboration, "Determination of the top-quark pole mass using $\mathrm{t\bar{t}} + 1$-jet events collected with the ATLAS experiment in 7 TeV pp collisions", *JHEP* **10** (2015) 121, doi:10.1007/JHEP10(2015)121, arXiv:1507.01769.

[27] D0 Collaboration, "Measurement of the inclusive $\mathrm{t\bar{t}}$ production cross section in $\mathrm{p\overline{p}}$ collisions at $\sqrt{s} = 1.96\,\text{TeV}$ and determination of the top quark pole mass", *Phys. Rev. D* **94** (2016) 092004, doi:10.1103/PhysRevD.94.092004, arXiv:1605.06168.

[28] ATLAS Collaboration, "Measurement of lepton differential distributions and the top quark mass in $\mathrm{t\bar{t}}$ production in pp collisions at $\sqrt{s} = 8\,\text{TeV}$ with the ATLAS detector", *Eur. Phys. J. C* **77** (2017) 804, doi:10.1140/epjc/s10052-017-5349-9, arXiv:1709.09407.

[29] CMS Collaboration, "Measurement of $\mathrm{t\bar{t}}$ normalised multi-differential cross sections in pp collisions at $\sqrt{s} = 13\,\text{TeV}$, and simultaneous determination of the strong coupling strength, top quark pole mass, and parton distribution functions", *Eur. Phys. J. C* **80** (2020) 658, doi:10.1140/epjc/s10052-020-7917-7, arXiv:1904.05237.

[30] U. Langenfeld, S. Moch, and P. Uwer, "Measuring the running top-quark mass", *Phys. Rev. D* **80** (2009) 054009, doi:10.1103/PhysRevD.80.054009, arXiv:0906.5273.

[31] J. Fuster et al., "Extracting the top-quark running mass using $\mathrm{t\bar{t}} + 1$-jet events produced at the Large Hadron Collider", *Eur. Phys. J. C* **77** (2017) 794, doi:10.1140/epjc/s10052-017-5354-z, arXiv:1704.00540.

[32] CMS Collaboration, "Running of the top quark mass from proton-proton collisions at $\sqrt{s} = 13\,\text{TeV}$", *Phys. Lett. B* **803** (2020) 135263, doi:10.1016/j.physletb.2020.135263, arXiv:1909.09193.

[33] S. Alioli et al., "A new observable to measure the top-quark mass at hadron colliders", *Eur. Phys. J. C* **73** (2013) 2438, doi:10.1140/epjc/s10052-013-2438-2, arXiv:1303.6415.

[34] G. Bevilacqua et al., "Top quark mass studies with $\mathrm{t\bar{t}j}$ at the LHC", *JHEP* **03** (2018) 169, doi:10.1007/JHEP03(2018)169, arXiv:1710.07515.

[35] ATLAS Collaboration, "Measurement of the top-quark mass in $\mathrm{t\bar{t}}$ + 1-jet events collected with the ATLAS detector in pp collisions at $\sqrt{s} = 8$ TeV", *JHEP* **11** (2019) 150, doi:10.1007/JHEP11(2019)150, arXiv:1905.02302.

[36] HEPData record for this analysis, 2022. doi:10.17182/hepdata.127990.

[37] CMS Collaboration, "Performance of the CMS Level-1 trigger in proton-proton collisions at $\sqrt{s} = 13$ TeV", *JINST* **15** (2020) P10017, doi:10.1088/1748-0221/15/10/P10017, arXiv:2006.10165.

[38] CMS Collaboration, "The CMS trigger system", *JINST* **12** (2017) P01020, doi:10.1088/1748-0221/12/01/P01020, arXiv:1609.02366.

[39] CMS Collaboration, "The CMS experiment at the CERN LHC", *JINST* **3** (2008) S08004, doi:10.1088/1748-0221/3/08/S08004.

[40] CMS Collaboration, "Technical proposal for the Phase-II upgrade of the Compact Muon Solenoid", CMS Technical Proposal CERN-LHCC-2015-010, CMS-TDR-15-02, 2015.

[41] CMS Collaboration, "Particle-flow reconstruction and global event description with the CMS detector", *JINST* **12** (2017) P10003, doi:10.1088/1748-0221/12/10/P10003, arXiv:1706.04965.

[42] CMS Collaboration, "Jet energy scale and resolution in the CMS experiment in pp collisions at 8 TeV", *JINST* **12** (2017) P02014, doi:10.1088/1748-0221/12/02/P02014, arXiv:1607.03663.

[43] CMS Collaboration, "Performance of missing transverse momentum reconstruction in proton-proton collisions at $\sqrt{s} = 13$ TeV using the CMS detector", *JINST* **14** (2019) P07004, doi:10.1088/1748-0221/14/07/P07004, arXiv:1903.06078.

[44] D. Bertolini, P. Harris, M. Low, and N. Tran, "Pileup per particle identification", *JHEP* **10** (2014) 059, doi:10.1007/JHEP10(2014)059, arXiv:1407.6013.

[45] CMS Collaboration, "Pileup mitigation at CMS in 13 TeV data", *JINST* **15** (2020) P09018, doi:10.1088/1748-0221/15/09/P09018, arXiv:2003.00503.

[46] CMS Collaboration, "ECAL 2016 refined calibration and Run 2 summary plots", CMS Detector Performance Summary CMS-DP-2020-021, 2020.

[47] CMS Collaboration, "Electron and photon reconstruction and identification with the CMS experiment at the CERN LHC", *JINST* **16** (2021) P05014, doi:10.1088/1748-0221/16/05/P05014, arXiv:2012.06888.

[48] CMS Collaboration, "Performance of the CMS muon detector and muon reconstruction with proton-proton collisions at $\sqrt{s} = 13$ TeV", *JINST* **13** (2018) P06015, doi:10.1088/1748-0221/13/06/P06015, arXiv:1804.04528.

[49] S. Frixione, P. Nason, and C. Oleari, "Matching NLO QCD computations with parton shower simulations: the POWHEG method", *JHEP* **11** (2007) 070, doi:10.1088/1126-6708/2007/11/070, arXiv:0709.2092.

[50] S. Frixione, G. Ridolfi, and P. Nason, "A positive-weight next-to-leading-order Monte Carlo for heavy flavour hadroproduction", *JHEP* **09** (2007) 126, doi:10.1088/1126-6708/2007/09/126, arXiv:0707.3088.

[51] S. Alioli, P. Nason, C. Oleari, and E. Re, "A general framework for implementing NLO calculations in shower Monte Carlo programs: the POWHEG BOX", *JHEP* **06** (2010) 043, doi:10.1007/JHEP06(2010)043, arXiv:1002.2581.

[52] NNPDF Collaboration, "Unbiased global determination of parton distributions and their uncertainties at NNLO and at LO", *Nucl. Phys. B* **855** (2012) 153, doi:10.1016/j.nuclphysb.2011.09.024, arXiv:1107.2652.

[53] NNPDF Collaboration, "Parton distributions from high-precision collider data", *Eur. Phys. J. C* **77** (2017) 663, doi:10.1140/epjc/s10052-017-5199-5, arXiv:1706.00428.

[54] T. Sjöstrand et al., "An introduction to PYTHIA8.2", *Comput. Phys. Commun.* **191** (2015) 159, doi:10.1016/j.cpc.2015.01.024, arXiv:1410.3012.

[55] CMS Collaboration, "Extraction and validation of a new set of CMS PYTHIA8 tunes from underlying-event measurements", *Eur. Phys. J. C* **80** (2020) 4, doi:10.1140/epjc/s10052-019-7499-4, arXiv:1903.12179.

[56] J. Alwall et al., "The automated computation of tree-level and next-to-leading order differential cross sections, and their matching to parton shower simulations", *JHEP* **07** (2014) 079, doi:10.1007/JHEP07(2014)079, arXiv:1405.0301.

[57] R. Frederix and S. Frixione, "Merging meets matching in MC@NLO", *JHEP* **12** (2012) 061, doi:10.1007/JHEP12(2012)061, arXiv:1209.6215.

[58] P. Artoisenet, R. Frederix, O. Mattelaer, and R. Rietkerk, "Automatic spin-entangled decays of heavy resonances in Monte Carlo simulations", *JHEP* **03** (2013) 015, doi:10.1007/JHEP03(2013)015, arXiv:1212.3460.

[59] E. Re, "Single-top Wt-channel production matched with parton showers using the POWHEG method", *Eur. Phys. J. C* **71** (2011) 1547, doi:10.1140/epjc/s10052-011-1547-z, arXiv:1009.2450.

[60] S. Alioli, P. Nason, C. Oleari, and E. Re, "NLO single-top production matched with shower in POWHEG: s- and t-channel contributions", *JHEP* **09** (2009) 111, doi:10.1088/1126-6708/2009/09/111, arXiv:0907.4076. [Erratum: doi:10.1007/JHEP02(2010)011].

[61] CMS Collaboration, "Investigations of the impact of the parton shower tuning in PYTHIA8 in the modelling of $\mathrm{t\bar{t}}$ at $\sqrt{s} = 8$ and 13 TeV", CMS Physics Analysis Summary CMS-PAS-TOP-16-021, 2016.

[62] CMS Collaboration, "Event generator tunes obtained from underlying event and multiparton scattering measurements", *Eur. Phys. J. C* **76** (2016) 155, doi:10.1140/epjc/s10052-016-3988-x, arXiv:1512.00815.

[63] P. Skands, S. Carrazza, and J. Rojo, "Tuning PYTHIA8.1: the Monash 2013 tune", *Eur. Phys. J. C* **74** (2014) 3024, doi:10.1140/epjc/s10052-014-3024-y, arXiv:1404.5630.

[64] M. L. Mangano, M. Moretti, F. Piccinini, and M. Treccani, "Matching matrix elements and shower evolution for top-pair production in hadronic collisions", *JHEP* **01** (2007) 013, doi:10.1088/1126-6708/2007/01/013, arXiv:hep-ph/0611129.

[65] S. Mrenna and P. Richardson, "Matching matrix elements and parton showers with HERWIG and PYTHIA", *JHEP* **05** (2004) 040, doi:10.1088/1126-6708/2004/05/040, arXiv:hep-ph/0312274.

[66] M. Czakon and A. Mitov, "Top++: A program for the calculation of the top-pair cross-section at hadron colliders", *Comput. Phys. Commun.* **185** (2014) 2930, doi:10.1016/j.cpc.2014.06.021, arXiv:1112.5675.

[67] M. Cacciari et al., "Top-pair production at hadron colliders with next-to-next-to-leading logarithmic soft-gluon resummation", *Phys. Lett. B* **710** (2012) 612, doi:10.1016/j.physletb.2012.03.013, arXiv:1111.5869.

[68] P. Bärnreuther, M. Czakon, and A. Mitov, "Percent level precision physics at the Tevatron: Next-to-next-to-leading order QCD corrections to $q\bar{q} \to t\bar{t} + X$", *Phys. Rev. Lett.* **109** (2012) 132001, doi:10.1103/PhysRevLett.109.132001, arXiv:1204.5201.

[69] M. Czakon and A. Mitov, "NNLO corrections to top-pair production at hadron colliders: the all-fermionic scattering channels", *JHEP* **12** (2012) 054, doi:10.1007/JHEP12(2012)054, arXiv:1207.0236.

[70] M. Czakon and A. Mitov, "NNLO corrections to top pair production at hadron colliders: the quark-gluon reaction", *JHEP* **01** (2013) 080, doi:10.1007/JHEP01(2013)080, arXiv:1210.6832.

[71] M. Beneke, P. Falgari, S. Klein, and C. Schwinn, "Hadronic top-quark pair production with NNLL threshold resummation", *Nucl. Phys. B* **855** (2012) 695, doi:10.1016/j.nuclphysb.2011.10.021, arXiv:1109.1536.

[72] M. Czakon, P. Fiedler, and A. Mitov, "Total top-quark pair-production cross section at hadron colliders through $\mathcal{O}(\alpha_S^4)$", *Phys. Rev. Lett.* **110** (2013) 252004, doi:10.1103/PhysRevLett.110.252004, arXiv:1303.6254.

[73] N. Kidonakis, "Two-loop soft anomalous dimensions for single top quark associated production with a W^- or H^-", *Phys. Rev. D* **82** (2010) 054018, doi:10.1103/PhysRevD.82.054018, arXiv:1005.4451.

[74] J. M. Campbell, R. K. Ellis, and C. Williams, "Vector boson pair production at the LHC", *JHEP* **07** (2011) 018, doi:10.1007/JHEP07(2011)018, arXiv:1105.0020.

[75] Y. Li and F. Petriello, "Combining QCD and electroweak corrections to dilepton production in the framework of the FEWZ simulation code", *Phys. Rev. D* **86** (2012) 094034, doi:10.1103/PhysRevD.86.094034, arXiv:1208.5967.

[76] GEANT4 Collaboration, "GEANT4—a simulation toolkit", *Nucl. Instrum. Meth. A* **506** (2003) 250, doi:10.1016/S0168-9002(03)01368-8.

[77] ATLAS Collaboration, "Measurement of the inelastic proton-proton cross section at $\sqrt{s} = 13\,\text{TeV}$ with the ATLAS detector at the LHC", *Phys. Rev. Lett.* **117** (2016) 182002, doi:10.1103/PhysRevLett.117.182002, arXiv:1606.02625.

[78] M. Cacciari, G. P. Salam, and G. Soyez, "The anti-k_T jet clustering algorithm", *JHEP* **04** (2008) 063, doi:10.1088/1126-6708/2008/04/063, arXiv:0802.1189.

[79] M. Cacciari, G. P. Salam, and G. Soyez, "FastJet user manual", *Eur. Phys. J. C* **72** (2012) 1896, doi:10.1140/epjc/s10052-012-1896-2, arXiv:1111.6097.

[80] CMS Collaboration, "Identification of heavy-flavour jets with the CMS detector in pp collisions at 13 TeV", *JINST* **13** (2018) P05011, doi:10.1088/1748-0221/13/05/P05011, arXiv:1712.07158.

[81] CMS Collaboration, "A deep neural network for simultaneous estimation of b jet energy and resolution", *Comput. Softw. Big Sci.* **4** (2020) 10, doi:10.1007/s41781-020-00041-z, arXiv:1912.06046.

[82] CMS Collaboration, "Measurement of the differential cross section for top quark pair production in pp collisions at $\sqrt{s} = 8$ TeV", *Eur. Phys. J. C* **75** (2015) 542, doi:10.1140/epjc/s10052-015-3709-x, arXiv:1505.04480.

[83] CMS Collaboration, "Measurement of double-differential cross sections for top quark pair production in pp collisions at $\sqrt{s} = 8$ TeV and impact on parton distribution functions", *Eur. Phys. J. C* **77** (2017) 459, doi:10.1140/epjc/s10052-017-4984-5, arXiv:1703.01630.

[84] CMS Collaboration, "Measurement of normalized differential $\mathrm{t\bar{t}}$ cross sections in the dilepton channel from pp collisions at $\sqrt{s} = 13$ TeV", *JHEP* **04** (2018) 060, doi:10.1007/JHEP04(2018)060, arXiv:1708.07638.

[85] CMS Collaboration, "Measurements of $\mathrm{t\bar{t}}$ differential cross sections in proton-proton collisions at $\sqrt{s} = 13$ TeV using events containing two leptons", *JHEP* **02** (2019) 149, doi:10.1007/JHEP02(2019)149, arXiv:1811.06625.

[86] L. Sonnenschein, "Analytical solution of $\mathrm{t\bar{t}}$ dilepton equations", *Phys. Rev. D* **73** (2006) 054015, doi:10.1103/PhysRevD.73.054015, arXiv:hep-ph/0603011. [Erratum: doi:10.1103/PhysRevD.78.079902].

[87] M. Abadi et al., "TensorFlow: large-scale machine learning on heterogeneous distributed systems", 2016. arXiv:1603.04467. Software available from https://www.tensorflow.org/.

[88] F. Chollet et al., "Keras", 2015. https://keras.io.

[89] J. Snoek, H. Larochelle, and R. P. Adams, "Practical Bayesian optimization of machine learning algorithms", 2012. arXiv:1206.2944.

[90] E. Brochu, V. M. Cora, and N. de Freitas, "A tutorial on Bayesian optimization of expensive cost functions, with application to active user modeling and hierarchical reinforcement learning", 2010. arXiv:1012.2599.

[91] F. Nogueira, "Bayesian optimization: open source constrained global optimization tool for Python", 2014. https://github.com/fmfn/BayesianOptimization.

[92] R. D. Cousins, "Generalization of chisquare goodness-of-fit test for binned data using saturated models, with application to histograms", 2013. http://www.physics.ucla.edu/~cousins/stats/cousins_saturated.pdf.

[93] Y. Ganin and V. Lempitsky, "Unsupervised domain adaptation by backpropagation", 2015. arXiv:1409.7495.

[94] J. Kieseler, K. Lipka, and S. Moch, "Calibration of the top-quark Monte Carlo mass", *Phys. Rev. Lett.* **116** (2016) 162001, doi:10.1103/PhysRevLett.116.162001, arXiv:1511.00841.

[95] F. James and M. Roos, "MINUIT—a system for function minimization and analysis of the parameter errors and correlations", *Comput. Phys. Commun.* **10** (1975) 343, doi:10.1016/0010-4655(75)90039-9.

[96] ATLAS and CMS Collaborations, and LHC Higgs Combination Group, "Procedure for the LHC Higgs boson search combination in summer 2011", Technical Report CMS-NOTE-2011-005, ATL-PHYS-PUB-2011-11, 2011.

[97] CMS Collaboration, "Precise determination of the mass of the Higgs boson and tests of compatibility of its couplings with the standard model predictions using proton collisions at 7 and 8 TeV", *Eur. Phys. J. C* **75** (2015) 212, doi:10.1140/epjc/s10052-015-3351-7, arXiv:1412.8662.

[98] ATLAS and CMS Collaborations, "Measurements of the Higgs boson production and decay rates and constraints on its couplings from a combined ATLAS and CMS analysis of the LHC pp collision data at $\sqrt{s} = 7$ and 8 TeV", *JHEP* **08** (2016) 045, doi:10.1007/JHEP08(2016)045, arXiv:1606.02266.

[99] J. S. Conway, "Incorporating nuisance parameters in likelihoods for multisource spectra", in *Proc. 2011 Workshop on Statistical Issues Related to Discovery Claims in Search Experiments and Unfolding (PHYSTAT 2011): Geneva, Switzerland, January 17–20, 2011*. 2011. arXiv:1103.0354. doi:10.5170/CERN-2011-006.115.

[100] CMS Collaboration, "Precision luminosity measurement in proton-proton collisions at $\sqrt{s} = 13$ TeV in 2015 and 2016 at CMS", *Eur. Phys. J. C* **81** (2021) 800, doi:10.1140/epjc/s10052-021-09538-2, arXiv:2104.01927.

[101] CMS Collaboration, "Performance of missing energy reconstruction in 13 TeV pp collision data using the CMS detector", CMS Physics Analysis Summary CMS-PAS-JME-16-004, 2016.

[102] CMS Collaboration, "Performance of the pile up jet identification in CMS for Run 2", CMS Detector Performance Note CMS-DP-2020-020, 2020.

[103] CMS Collaboration, "Performance of the CMS muon trigger system in proton-proton collisions at $\sqrt{s} = 13$ TeV", *JINST* **16** (2021) P07001, doi:10.1088/1748-0221/16/07/P07001, arXiv:2102.04790.

[104] S. Argyropoulos and T. Sjöstrand, "Effects of color reconnection on $\mathrm{t\bar{t}}$ final states at the LHC", *JHEP* **11** (2014) 043, doi:10.1007/JHEP11(2014)043, arXiv:1407.6653.

[105] J. R. Christiansen and P. Z. Skands, "String formation beyond leading colour", *JHEP* **08** (2015) 003, doi:10.1007/JHEP08(2015)003, arXiv:1505.01681.

[106] M. G. Bowler, "$\mathrm{e^+e^-}$ production of heavy quarks in the string model", *Z. Phys. C* **11** (1981) 169, doi:10.1007/BF01574001.

[107] C. Peterson, D. Schlatter, I. Schmitt, and P. M. Zerwas, "Scaling violations in inclusive $\mathrm{e^+e^-}$ annihilation spectra", *Phys. Rev. D* **27** (1983) 105, doi:10.1103/PhysRevD.27.105.

[108] R. Barlow and C. Beeston, "Fitting using finite Monte Carlo samples", *Comput. Phys. Commun.* **77** (1993) 219, doi:10.1016/0010-4655(93)90005-w.

[109] S. Alioli, S. Moch, and P. Uwer, "Hadronic top-quark pair-production with one jet and parton showering", *JHEP* **01** (2012) 137, doi:10.1007/JHEP01(2012)137, arXiv:1110.5251.

[110] S. Alekhin, J. Blümlein, and S. Moch, "NLO PDFs from the ABMP16 fit", *Eur. Phys. J. C* **78** (2018) 477, doi:10.1140/epjc/s10052-018-5947-1, arXiv:1803.07537.

[111] T.-J. Hou et al., "Progress in the CTEQ-TEA NNLO global QCD analysis", 2019. arXiv:1908.11394.

[112] G. Bevilacqua, H. B. Hartanto, M. Kraus, and M. Worek, "Off-shell top quarks with one jet at the LHC: a comprehensive analysis at NLO QCD", *JHEP* **11** (2016) 098, doi:10.1007/JHEP11(2016)098, arXiv:1609.01659.

[113] S. Alioli et al., "Phenomenology of $t\bar{t}j + X$ production at the LHC", *JHEP* **05** (2022) 146, doi:10.1007/JHEP05(2022)146, arXiv:2202.07975.